A Single-Objective Light-Sheet Microscope with 200 nm-Scale Resolution.

Etai Sapoznik[1,2], Bo-Jui Chang[1], Robert J. Ju[3], Erik S. Welf[1,2], David Broadbent[4], Alexandre F. Carisey[5], Samantha J. Stehbens[3], Kyung-min Lee[6], Arnaldo Marín[6], Ariella B. Hanker[6], Jens C. Schmidt[4,7], Carlos L. Arteaga[6], Bin Yang[8], Rory Kruithoff[9], Doug P. Shepherd[9], Alfred Millett-Sikking[10], Andrew G. York[10], Kevin M. Dean[1*], Reto Fiolka[1,2*]

1 – Department of Cell Biology, University of Texas Southwestern Medical Center, Dallas, TX, USA.

2 – Department of Bioinformatics, University of Texas Southwestern Medical Center, Dallas, TX, USA.

3 – Institute for Molecular Bioscience, University of Queensland, St Lucia, Queensland, Australia.

4 – Institute for Quantitative Health Sciences and Engineering, Michigan State University, East Lansing, MI, USA.

5 – William T. Shearer Center for Human Immunobiology, Baylor College of Medicine and Texas Children's Hospital, Houston, TX, USA.

6 – Harold C. Simmons Comprehensive Cancer Center and the Department of Internal Medicine, University of Texas Southwestern Medical Center, Dallas, TX, USA.

7 - Department of Obstetrics, Gynecology, and Reproductive Biology, Michigan State University, East Lansing, MI, USA.

8 – Chan Zuckerberg Biohub, San Francisco, CA, USA.

9 – Department of Physics and the Center for Biological Physics, Arizona State University, Tempe, AZ, USA.

10 – Calico Life Sciences LLC, South San Francisco, CA, USA.

***Corresponding authors:**

Kevin M. Dean - kevin.dean@utsouthwestern.edu

Reto Fiolka - reto.fiolka@utsouthwestern.edu

Abstract:

We present a single-objective light-sheet microscope, also known as an oblique-plane microscope, that uses a bespoke glass-tipped tertiary objective and improves the resolution, field of view, usability, and stability over previous variants. Owing to its high numerical aperture optics, this microscope achieves the highest lateral resolution in light-sheet fluorescence microscopy, and its axial resolution is similar to that of Lattice Light-Sheet Microscopy. Given this performance, we demonstrate high-resolution imaging of clathrin-mediated endocytosis, vimentin, the endoplasmic reticulum, membrane dynamics, and natural killer cell-mediated cell death. Furthermore, we image biological phenomena that would be otherwise challenging or impossible to perform in a traditional light-sheet microscope geometry, including cell migration through a confined space within a microfluidic device, photoactivation of PI3K, and diffusion of cytoplasmic rheological tracers at a volumetric rate of 14 Hz.

Introduction

Light-sheet fluorescence microscopy (LSFM) first generated significant interest in the biological community as a result of its ability to image developing embryos with single cell resolution, inherent optical sectioning, and high temporal resolution (Huisken, 2004). Since then, LSFM has undergone a revolution, and depending on the optical configuration, can now routinely image biological systems that range from reconstituted macromolecular complexes (Keller et al., 2007) to intact organs and organisms (Chakraborty et al., 2019; Voigt et al., 2019). Unlike other microscope modalities that are used to image three-dimensional specimens (e.g., confocal), LSFM only delivers light to the in-focus portion of the specimen, and therefore substantially decreases the illumination burden on the sample. Further, light-sheet excitation combines powerfully with the million-fold parallelization afforded by modern scientific cameras, permitting massive reductions in illumination intensities without compromising the signal to noise ratio, which significantly reduces the rate of photobleaching and phototoxicity. Consequently, LSFM permits imaging of biological specimens for 1000's of volumes (Dean et al., 2017).

Nevertheless, despite its advantages over other imaging modalities, its widespread adoption remains limited. In part, this is due to the slow adoption of cutting-edge LSFM systems by commercial entities, and therefore the requirement for expert assembly, maintenance, alignment, and operation of LSFM instruments. Complicated sample preparation is an additional problem, as the orthogonal geometry of LSFM systems sterically occludes standard imaging dishes, multi-well plates, and instead, can require that samples be mounted on ~5 mm diameter coverslips (Chen et al., 2014) or within low melting point agarose (Chhetri et al., 2015). For the highest resolution LSFM systems, the reliance on high-NA water-dipping objectives places the sample in direct contact with non-sterile optical surfaces, which compromises long-term imaging. And lastly, these matters are made worse because modern LSFM systems lack many of the modalities that render microscopy routinely useful for non-experts, including sample environmental control, and laser-based autofocusing schemes.

There is however one form of LSFM, referred to as single-objective light-sheet microscopy or oblique plane microscopy, that avoids these complications (Dunsby, 2008). Unlike most LSFMs that require separate illumination and detection objectives, a single-objective light-sheet microscope, as the name suggests, uses only one objective at the specimen. As such, a single-objective light-sheet microscope can be assembled using a standard inverted or upright microscope geometry and is entirely compatible with traditional forms of sample mounting, environment control, and laser-based auto-focusing. In single-objective light-sheet microscopy, a highly inclined light-sheet is launched from a primary objective into the biological specimen **(Figure 1A)**, and the resulting fluorescence from this sheet is captured by the primary objective, relayed in an aberration-free remote focusing (Botcherby et al., 2012) format to a secondary objective, which creates a 3D replica of the detected fluorescence that is then imaged off-axis by a tertiary objective onto a camera **(Figure 1B)**.

To date, most single-objective light-sheet microscopes have had low optical resolution because the tertiary objective fails to capture the high angle rays that are launched from the secondary objective. Nevertheless, it was recently demonstrated that a single-objective light-sheet microscope can achieve ~300 nm scale resolution by combining air and water objectives with a coverslip-walled immersion chamber (Yang et al., 2019). Here, as light rays travel from a low to a high refractive index medium (e.g., air and water, respectively), they are refracted at the coverslip interface towards the tertiary objective in a manner that compresses the optical cone of light, and thereby permits capture of the higher angle rays (Yang et al., 2019). Nevertheless, aligning this chamber, which requires that the coverslip be placed at the proper distance and angle relative to both the secondary and tertiary objectives, while maintaining a proper water immersion for the tertiary objective, although feasible, is quite technically challenging. To mitigate these challenges, a bespoke glass-tipped tertiary objective was recently developed that eliminates the need for an immersion chamber and further improves the resolution of the imaging system due to the high refractive index of glass **(Figure 1B)** (Millett-Sikking et al., 2019). In theory, and according to numerical simulations and preliminary measurements, this new optical design has only small losses in numerical aperture or resolution from its primary objective (Millett-Sikking et al., 2019). Here, we built a high-NA single-objective light-sheet microscope equipped with the glass-tipped tertiary objective and characterize its optical resolution, imaging speed, field size, and light-throughput, and demonstrate instrument performance by imaging in a traditional inverted microscopy format clathrin-mediated endocytosis, cell migration, and NK cell mediated cytotoxicity. Lastly, we image processes that would otherwise be challenging to accomplish with a traditional light-sheet microscope, including nuclear rupture as melanoma cells migrate through tightly confined spaces in a microfluidic device and optogenetic activation of PI3K.

Results

Microscope Design

We present a single-objective light-sheet microscope that leverages the maximum resolving power of a new glass-tipped tertiary objective (Millett-Sikking et al., 2019). In this design, a high-NA primary objective (100X, NA 1.35) with an angular aperture of ~70 degrees is matched to a high-NA secondary air objective (40X, NA 0.95) possessing a similarly high angular range. The tertiary imaging system, consisting of the glass-tipped objective (Millett-Sikking et al., 2019), tube lens, filter wheel, and a scientific CMOS camera, is tilted by 30 degrees relative to the optical axis of the secondary objective. Other angles are possible (between 0-45 degrees), so long as the angle is matched to that of the light-sheet in sample space **(Figure 1B)**. Inspired by tilt-invariant imaging systems (Kumar et al., 2018; Voleti et al., 2019; Yang et al., 2019), we designed the single-objective light-sheet microscope with a high-speed galvanometer mirror conjugate to both the primary and secondary objective pupils, which allows for rapid light-sheet scanning in sample space, and rapid emission descanning prior to detection with the camera (**Supplementary Figure 1**). To achieve aberration- and distortion-free imaging, the optical train was carefully designed to properly map the two pupils, and tube and scan lenses were selected that maximized the diffraction-limited field of view. To improve the accessibility of the system, it was built in a standard inverted microscope format, which features a motorized sample stage, objective and sample heating, and a temperature and CO_2-regulated environmental chamber. Because the mirror galvanometer is the only moving part, and only a portion of the camera is necessary to detect the descanned fluorescence (~256 x 2048), this microscope allows very high imaging rates (~800 planes per second).

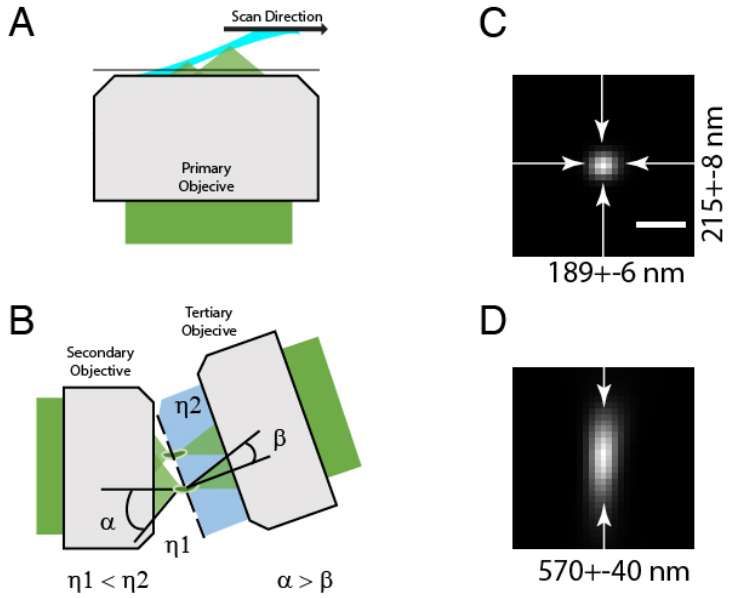

Figure 1. Optical principle and performance. (A) The light-sheet, shown in light blue, is launched from the primary objective at a 30-degree oblique illumination angle, and the resulting fluorescence cones of light,

shown in green, are collected by the same objective. (B) A replica of the fluorescence collected from the primary objective is formed by the secondary objective at the refractive index interface created by the glass-tipped objective. As the light travels from a region of low refractive index (η_1, air) to high refractive index (η_1, glass), the optical cone of light is compressed from an angle of α to β. (C) Point spread function after iterative deconvolution at the center of the field of view. Values indicate mean and standard full width half maximum for 100 nm beads (N = 14) imaged over a 60 x 60 micron field of view. (D) Corresponding axial view of the point spread function shown in (C). Scale Bar in (C): 500 nm.

We designed the microscope with three laser lines (488, 561, 642 nm) that can be flexibly reconfigured with two motorized flip mirrors and illuminate the cells in either an oblique light-sheet, widefield, or laser-scanned diffraction-limited geometry. The oblique light-sheet path and the two epi light paths are combined with a polarizing beam splitter. The light-sheet illumination is formed with a cylindrical lens and its thickness is controlled with a variable slit aperture. Such a 1D light-sheet offers 100% spatial duty cycle, which reduces photo-toxicity and photobleaching compared to light-sheets that are obtained by laterally scanning a 2D laser focus (Keller et al., 2008). To minimize shadow artifacts, a resonant galvanometric mirror, located in a plane conjugate to the sample is used to rapidly pivot the light-sheet in sample space **(Supplementary Figure 2 and 3)** (Huisken and Stainier, 2007). The lateral position of the light-sheet is controlled by a dedicated galvanometric mirror, and its incidence angle is adjusted with a manual translation stage **(Supplementary Figure 3**. The path for widefield and point laser scanning illumination features an additional galvanometric mirror, which together with the z-galvanometer, can be used to illuminate the cell with arbitrary 2D patterns of light **(Supplementary Figure 4 and 5, Supplementary Movie 1)**. Here, we use this path to perform optogenetic stimulation, but it could also be used for fluorescence recovery after photobleaching or photoactivation. In this mode, the 488 nm laser is used for stimulation, and the 561 and 642 nm lasers are used for light-sheet imaging. For widefield imaging, we illuminate the sample with a ~200-micron diameter collimated beam and detect fluorescence with a secondary camera that is located immediately after the first tube lens. Each laser line is controlled with a fast-mechanical shutter (**See Methods**).

Instrument Characterization.

Scanning of the oblique illumination beam was performed with a high-speed galvanometer mirror, and the fluorescence was descanned onto a thin portion (e.g., 256 x 2048 pixels) of a scientific CMOS camera. Because the mirror galvanometer can be scanned at ~2 kHz, the camera sensor, or the sample brightness, was rate limiting, and we routinely imaged at ~800 planes per second. To measure the resolution, 100 nm green fluorescent beads were immobilized to a #1.5 glass coverslip with poly-L-Lysine and imaged volumetrically in a laser-scanning light-sheet format. In the central field of view (60x60 microns), we measured a lateral resolution of 284 ± 12 nm normal to the scan direction, a lateral resolution of 328 ±

14 nm in the scan direction, and a 823 ± 81 nm resolution (mean and standard deviation of the Full Width Half Maximum (FWHM), N=14 measurements). For comparison, the X, Y, and Z resolution of the primary objective when imaged in a traditional widefield format was 243 ± 11 nm, 242 ± 15 nm, and 604 ± 31 nm, respectively. Deconvolution can be applied to improve the resolution, which resulted in a resolution gain of ~$2^{0.5}$ after 20 iterations. This yielded a FWHM of 189 ± 6 nm normal to the scan direction, 215 ± 8 nm parallel with the scan direction, and 570 ± 40 nm in the axial direction. A corresponding point spread function is shown in **Figure 1C and D**. The ~200 nm-scale lateral resolution and 600-700 nm-scale axial resolution is maintained over a 10-micron depth in z and over a lateral field of view of ~100 microns (**Supplementary Figure 6**). A larger field of view, in our case limited by the camera to 230 microns, can still be imaged, but imaging performance slowly degrades towards the edges (**Supplementary Figure 6**). While some degradation of the optical performance is expected when tilting the tertiary objective, it is still an active matter of investigation if this can be improved.

Given the large number of optics in the emission path, we were also concerned that absorption and spurious reflections could result in a diminished collection efficiency. To evaluate this, we measured the light throughput of the optical system using a 543 nm HeNe laser in transmission. In the absence of the primary objective, we measured a 71% decrease in laser power prior to imaging with the sCMOS camera. These losses are in part offset by the significantly greater NA of primary objective relative to other light-sheet microscopes. For example, we expect a NA 1.35 objective to collect ~1.7 and ~3.6 times more photons than a NA 1.1 or NA 0.8 objective, respectively. For particularly dim specimens, the microscope could be designed to operate in a sample scanning format (albeit at a slower image acquisition rate) that reduces the number of optical interfaces necessary and is therefore only accompanied by a 51% decrease in transmission (See Supporting Methods).

Biological Imaging of Clathrin Mediated Endocytosis, Vimentin, and Membrane Dynamics.

To evaluate microscope performance on biological specimens, we first imaged the endoplasmic reticulum in U2OS osteosarcoma cells **(Figure 2A, and Supplementary Movie 2)**. Endoplasmic reticulum tubules were highly dynamic, and unlike methods that rely on imaging slightly out of a total internal reflection geometry (Li et al., 2015), could be imaged with high-resolution throughout the entire cell volume. We also imaged genomically tagged vimentin in retinal pigment epithelial cells. Vimentin is an intermediate filament that is often associated with the epithelial to mesenchymal transition and is hypothesized to reinforce polarity cues through crosstalk in the microtubule, actin, and integrin-mediated adhesion cellular systems. Here, vimentin appeared as moderately dynamic filamentous structures that extended from a perinuclear localization to the cell periphery **(Figure 2B, and Supplementary Movie 3)**. In regions where the cell was actively protruding, the vimentin cytoskeleton experienced retrograde flow in a manner analogous to actin. Vimentin filaments occupied both the apical and basal sides of the cell, as is visible in an axial cross-section through the cell **(Figure 2C).** To evaluate our ability to image more dynamic processes, we imaged clathrin

mediated endocytosis in retinal pigment epithelial cells that were labeled with the clathrin adapter protein AP2 fused to GFP **(Figure 2D and E, Supplementary Movies 4 and 5)**. Endocytosis could be observed through time, with individual endocytic pits appearing as point-like structures that initialized on the plasma membrane, locally diffused, and then disappeared upon scission and release into the cytosol. We also imaged PIP3 formation, the product of phosphoinositide 3-kinase activity in long-term estrogen-deprived MCF7 human breast cancer cells with the Akt-PH-GFP biosensor. MCF7 cells harbor an activating mutation in *PIK3CA*, the gene encoding PI3Kα and long-term estrogen deprived MCF7 cells display hyper-activation of PI3K pathway compared to parental MCF7 cells (Miller et al., 2010). PI3K activity is associated with a diverse range of cellular phenomena, including migration, proliferation, survival, and more, and PI3Kα is clinically targeted in hormone receptor-positive breast cancers harboring *PIK3CA* mutations (Andre et al., 2019). Here, cells displayed membrane ruffles with heightened PI3K activity, and this activity was abrogated upon inhibition of PI3K with the FDA-approved PI3Kα inhibitor alpelisib (**Supplementary Figure 7**). Lastly, we imaged MV3 melanoma cells tagged with a membrane marker. These cells displayed numerous dynamic cellular protrusions, including blebs and filopodia, which extended away from the coverslip that otherwise could not have been observed without the spatiotemporal resolution afforded by single-objective light-sheet microscopy (**Figure 2F-H, Supplementary Movie 6**). In particular, we could observe short lived buckling events of filopodia (**Supplementary Figure 8).**

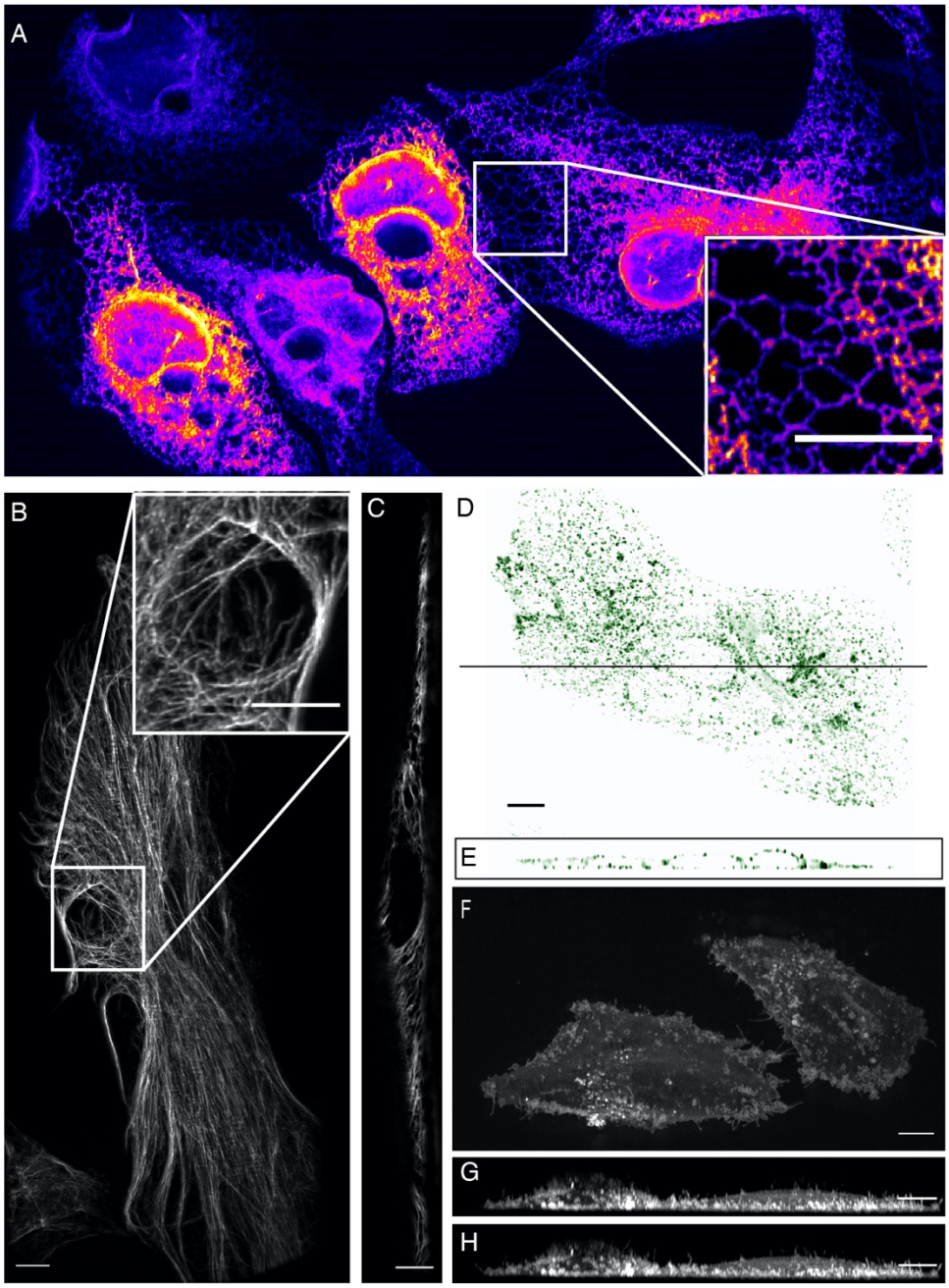

Figure 2. High-resolution biological imaging. (A) Endoplasmic reticulum in U2OS cells. Inset shows fine details in the dense, tubulated network. (B) Vimentin in RPE hTERT cells. (C) Single slice through vimentin network. (D) Lateral and (E) axial view of clathrin-mediated endocytosis in ARPE cells. (F) Cortical blebs in MV3 melanoma cells. (G) Cross-section through MV3 cells at the 6th and (H) 12th time point. All scale bars are 10 microns.

Natural Killer Cell Mediated Cytotoxicity

Studying cell-cell interactions is particularly suitable for this microscope as it provides an ideal blend of resolution, speed, and large field of view. This facilitates the acquisition of simultaneous, randomly occurring and short-lived events between multiple cell populations. To demonstrate its potential, we imaged the formation of cytolytic immune synapse (IS) between cytotoxic and cancer cells. Natural Killer (NK) cells are one of the main components of the innate response of the immune system, and these cells have the unique ability to directly recognize and destroy virally infected or transformed cells via a multipurpose interface with the target cell. A key feature of the formation of the IS (Mace et al., 2014) is the accumulation of F-actin at the interface between the two cell types. Although the formation (Mace and Orange, 2014) and the dynamism (Carisey et al., 2018) of this actin-based network are critical to ensure the productive outcome of the cytotoxic process, the interplay between the plasma membranes of the two cells remains poorly understood, in part because much of the work has been performed on ligand-coated artificial surfaces (Carisey et al., 2018; Marrack et al., 2011). Here we show how the cortical actin cytoskeleton of the NK cell (**Figure 3, Supplementary Movie 7**) organizes at the IS and follows a cortical, retrograde flow away from the synapse, along the cell axis, similarly to what has been seen in T cells (Chen et al., 2014; Ritter et al., 2015). More interestingly, long tethers of membrane are pulled from the target cell (plasma membrane marker derived from Lck fused with Venus FP) along with the actin flow. This could be a direct visualization of the first stage of trogocytosis, an important consequence of the mechanotransduction occurring at the IS that can lead to hypo-responsiveness in NK cell (Miner et al., 2015). With the most recent work performed on cytolytic T cells emphasizing the crucial role of tension transmitted through the ligand-receptor axis on the organization of the underlying actin cytoskeleton (Kumari et al., 2020), it seems more necessary than ever to use new approaches that move the field away from the classical model of ligand-coated surfaces. The fast and live-cell friendly volumetric imaging method described here allows us to directly address new challenges in a more relevant context.

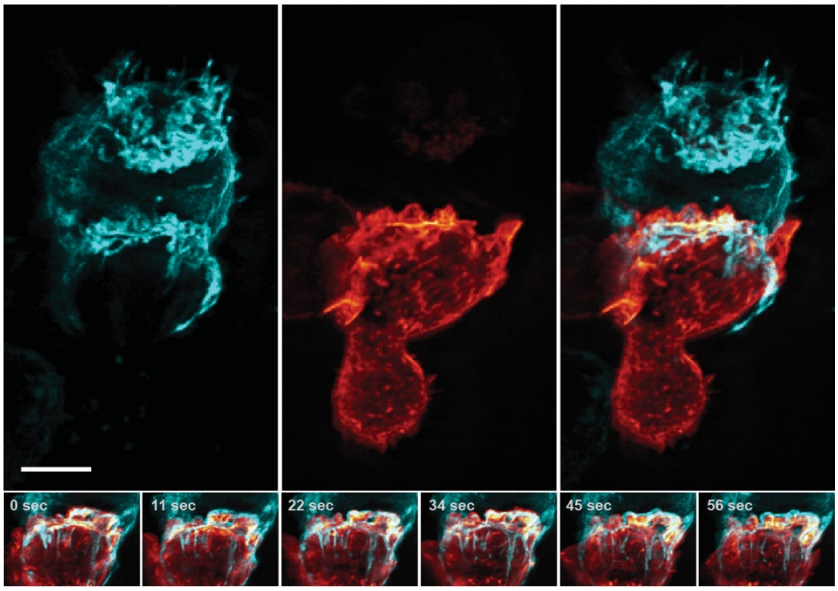

Figure 3. Formation of an immunological synapse between a Natural Killer cell and a target cell. A NK-92 natural killer cell line expressing Life-Act-mScarlet (center, orange) comes in contact with a K562 leukemic cell expressing Lck-mVenus, which is myristolyated and localizes to the plasma membrane (left, cyan). Right panel: overlay of NK-92 and K562 cells during the formation and maturation stages of the immunological synapse. Upon formation of the synapse, centrifugal flows driven by the NK-92 cell results in displacement of the K562 cellular membrane highlighted by the presence of membrane tethers, visible in the left panel and emphasized in the color merged frame sequence (bottom). Data is shown as maximum intensity projection. Time interval 11.33 seconds, scale bar, 5 microns.

Imaging in Biological Microchannels – Microtubules & Nuclear Rupture.

Cells migrating through 3D microenvironments such as dense stromal tissues are rate-limited by the cross-sectional diameter of their nucleus. This nuclear threshold defines the ability for cells successfully migrate through tight pores in between matrix fibers within the 3D microenvironment (Wolf et al., 2013). The study of the adaptive mechanisms developed by cells to effectively navigate these complex environments is key to our understanding of multiple different biological disciplines spanning development, cancer metastasis and homeostatic processes such as wound healing.

Our understanding of the mechanisms governing nuclear movement and protection in 3D environments is emerging. We now know that nuclear constriction can result in nuclear herniation, rupture and DNA damage (Denais et al., 2016; Raab et al., 2016). Unfortunately, observing these events *in vivo* still remains technically challenging and low-throughput. Microfluidic devices provide an accurate and reproducible model of this phenomenon whereby cells can be subjected to user-defined mechanical constrictions of unique sizes and shapes that serve to recapitulate the biological microenvironment(Garcia-Arcos et al., 2019). Using this system allows us to interrogate the cellular mechanisms of nuclear rupture,

DNA damage and repair (Raab et al., 2016). However, volumetric imaging of this biological process requires both high spatial and temporal resolution, and to date, confocal microscopes are accompanied with too much phototoxicity to permit longitudinal observation of migration through confinement microchannels. While light sheet microscopy is an attractive alternative to confocal microscopy, owing to their glass-polydimethylsiloxane sandwich geometry, microfluidic devices are not compatible with traditional light-sheet microscopes that use water dipping objectives and require an orthogonal illumination and detection geometry. Using our single-objective light-sheet microscope, we were able to circumvent this, volumetrically imaging nuclear positioning and microtubule dynamic morphology as cells navigated mechanical constrictions **(Figure 4A, Supplementary Movie 8)**. Here, the microfluidic device was ~4-microns tall, consisting of an array of large and smaller circular posts, with constriction junctions of 2.5 μm and 2 μm, respectively **(Figure 4B)**. Cells generated long, microtubule-rich protrusions, and migrated in a polarized manner. The nucleus was visibly compressed when viewed in the axial direction (**Figure 4C**), and upon closer inspection, appeared to be surrounded with microtubules **(Figure 4D)** on both the apical and basal surfaces of the nucleus (**Figure 4E**).

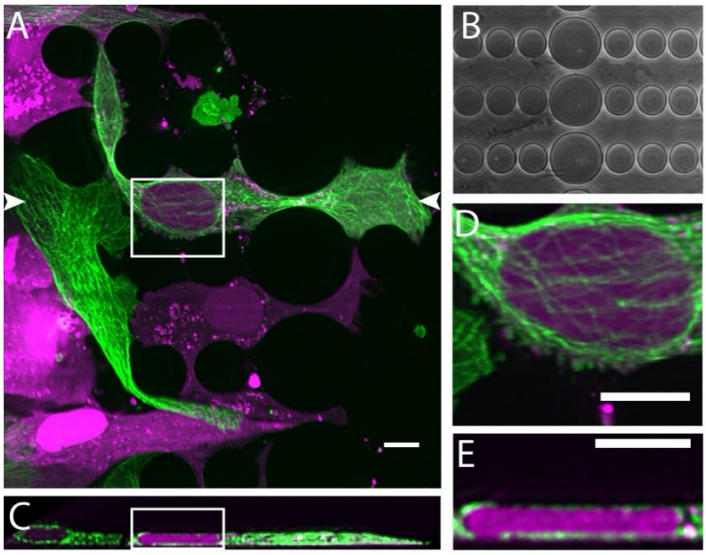

Figure 4. Cell migration through PDMS micro-confinement channels. (A) 1205Lu metastatic melanoma cells endogenously expressing eGFP-α-tubulin tagged microtubules with CRISPR (green) and a nuclear-localized red fluorescent protein (3x NLS mScarlet-I; magenta), migrating through a PDMS microchannel device. Scale bar 10 microns. (B) Brightfield image of microfluidic device, where cells migrate in the horizontal dimension and squeeze between the pillars (large pillars are separated by 2.5 microns, and small pillars are separated by 2 microns). (C) Axial cross-section of cells in a microchannel device shows top-down nuclear confinement as cells migrate through 4-micron tall channels. (D) Microtubule protofilaments wrap around both the basal and apical surfaces of the cell when migrating through confined spaces. Scale bar 10 microns. (E) Zoom of the region shown in C. Scale bar 10 microns.

High-speed imaging of calcium transduction and cytoplasmic flow with genetically encoded multimeric nanoparticles.

For three-dimensional imaging, most microscopes require scanning heavy optical components (e.g., objectives), which limits the volumetric image acquisition rate owing to the low-frequency limitations of modern positioning devices. Nevertheless, because the single-objective light-sheet microscope described here adopts a tilt-invariant illumination architecture with a galvanometer-based scan-descan optical path, camera framerate-limited imaging is possible (Kumar et al., 2018; Voleti et al., 2019; Yang et al., 2019). Owing to this, we sought to image fast biological processes, including calcium wave propagation and the rapid diffusion of cytoplasmic tracers. For the former, we used the small molecule calcium sensor Fluo-3, and imaged rat primary cardiomyocytes at a volumetric image acquisition rate of 10.4 Hz (**Figure 5A, Supplementary Movie 9**). Here, imaging was sufficiently fast to observe calcium translocation during spontaneous cardiomyocyte contraction. Such imaging can improve the understanding of single cell calcium waves which is important for cardiac physiology and disease (Gilbert et al., 2020).

To evaluate the rheological properties of the cytoplasm, we used genetically encoded multimeric nanoparticles (GEMs), which are self-forming icosahedral assemblies of fluorescent proteins that act as inert cytoplasmic tracers. The GEMs appeared as bright puncta within the cell that rapidly diffused, and we were able to image and track these tracers over 100 time points at a volumetric image acquisition rate of 13.7 Hz using the particle detection and tracking software uTrack (Jaqaman et al., 2008) (**Figure 5B, Supplementary Movie 10**). Such tracking can help us understand the diffusion regime in various cell domains. This can be used to assess known factors in affecting GEMs movement, such as ribosome crowding and its effect on cell phenotype such as changes in cell mechanics (Delarue et al., 2018; Hannezo and Heisenberg, 2019).

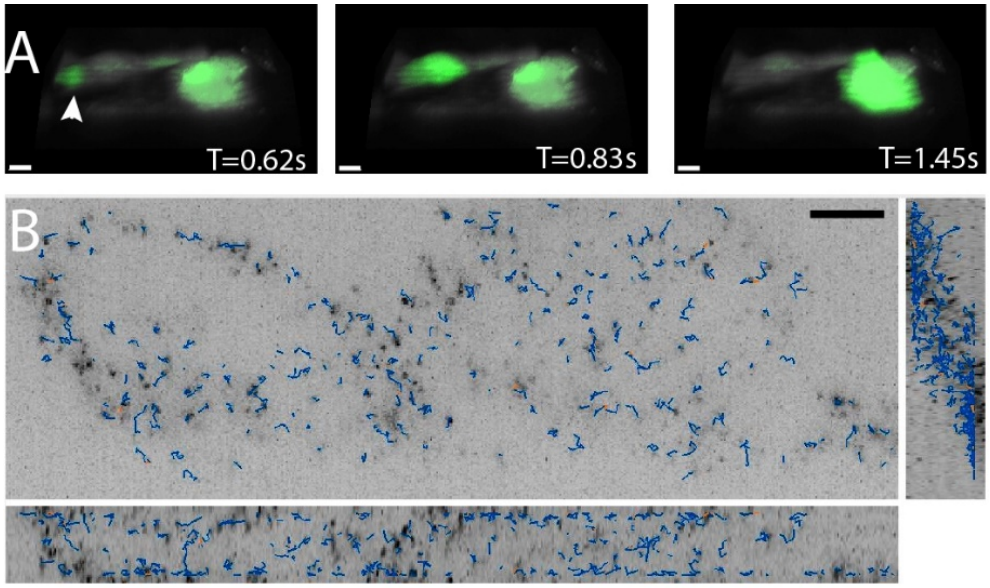

Figure 5. High-speed volumetric imaging of calcium waves and genetically encoded multimeric nanoparticles. (A) Primary rat cardiomyocytes were labeled with the small molecule sensor, Fluo-3, and imaged at 10.4 Hz. Scale Bar: 10 microns. (B) Imaging rheological tracers in the mammalian cytosol at 13.7 Hz. Scale Bar: 10 microns.

Photoactivation – PI3K *activation.*

In addition to its effects on cell proliferation and survival, PI3K drives cell shape change and migration (Welf et al., 2012). Leveraging the photoactivation arm of the microscope, we deployed an optogenetic tool that locally recruits the iSH2 (Idevall-Hagren et al., 2012) domain of PI3K to the membrane, thus increasing local PI3K activity that drives cell edge dynamics (**Figure 6A-C**). The ability to acquire high resolution 3-D images during photoactivation revealed that the more dominant effect of local PI3K activity is actually dorsal cell ruffles, which propagate towards the cell nucleus in a retrograde fashion (**Figure 6, Supplementary Movie 10**) (Asthagiri et al., 2018). Our 3D imaging capabilities also enabled us to observe the appearance of ventral cell buckling and separation from the coverslip due to PI3K activation (**Supplementary Figure 9, Supplementary Movie 11**), a phenomenon which to our knowledge has not been observed before.

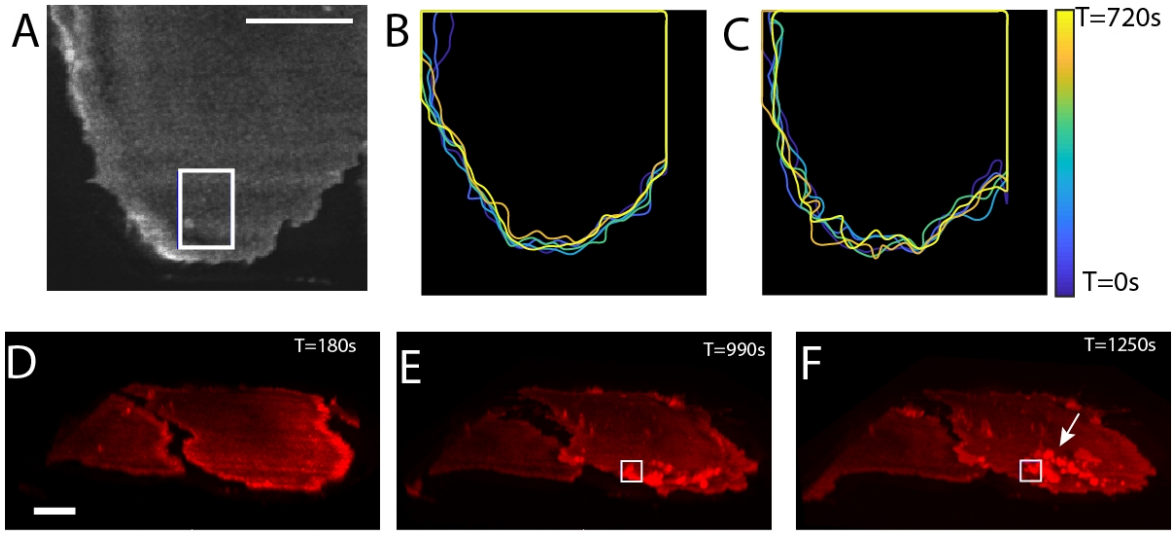

Figure 6. Using PI3K optogenetics to induce morphodynamic changes in melanoma MV3 cells. Cell sub-region (white rectangle) (A) was point-scanned with 488 nm laser for photo-activation while the whole cell was imaged with 647nm using SNAP-AktPH and SNAP-Cell 647 SiR. Cell boundary changes show the

difference in cell edge activity between the first 12 minutes with no activation (B) and 12 minutes of activation (C); Three-dimensional rendering shows cell response in time points prior to (D) and during photoactivation (E, F). Time interval 30 seconds, scale bar 10 microns.

Discussion

High-resolution light-sheet microscopy has yet to be widely adopted in biological laboratories and core facilities owing to routine problems with sample drift, contamination, and lack of user friendliness. Here, we show that a single-objective light-sheet microscope with customized optics overcomes these challenges, and combines the ease of traditional sample mounting, sterile environmental control, and multi-position stage control with the gentle, subcellular imaging afforded by selective plane illumination. For example, cells were easily identified in a traditional epi-fluorescence format prior to imaging in the single-objective light-sheet mode, the focus was maintained with readily available hardware solutions, and the environment remained sterile with CO_2, humidity, and temperature control. In addition to its ease of use, the single-objective light-sheet microscope described here delivers spatial and temporal resolution that is on par or exceeds the best-in-class light-sheet microscopes, including Lattice Light-Sheet Microscopy (Chen et al., 2014) or pSPIM (Dean et al., 2017).

This is in stark contrast to previous generations of single-objective light-sheet microscopes (Bouchard et al., 2015; Dunsby, 2008; Kumar et al., 2011), which provided only moderate spatial resolution. This revolution in single-objective light-sheet microscopy performance was triggered by the insight that one could combine a high-NA (~0.9) air secondary objective with a high-NA (~1.0) water-immersion tertiary objective (Yang et al., 2019). In such a system, the refractive index interface between the two objectives compresses and refracts the optical cone of light towards the tertiary objective and improves both sensitivity and resolution of the entire imaging system. In this work, we take this concept to its logical extreme with an optimized optical train, and we replace the tertiary objective (and its water chamber and coverslip) with a solid immersion objective that eases alignment, and more efficiently compresses and refracts the optical cone of light (Millett-Sikking et al., 2019). We characterize the performance of this system and demonstrate that even without implementing super-resolution concepts (e.g., STORM/PALM, SIM, STED), it has the highest lateral resolving power (~200 nm) in light-sheet microscopy. Indeed, owing to the narrow depth of focus provided by the optical design, the axial resolving power (~550 nm) is similar to what can be achieved with the squared lattice illumination in Lattice Light-Sheet Microscopy, except here it is achieved with a high contrast Gaussian light-sheets. And lastly, because the volumetric image acquisition rate is not limited by piezoelectric scanning of either the sample or the objective, but rather a high-speed galvanometric mirror, very high temporal resolution is possible. Here, we demonstrated volumetric subcellular imaging at rates of 10 Hz, which permitted tracking of intracellular flows and calcium propagation. To demonstrate its utility, we performed a variety of imaging tasks that would be hard or impossible to perform on a traditional light-sheet microscope, including imaging in a microfluidic channel, optogenetics, and video-rate volumetric

subcellular imaging. Indeed, the stage-scanning variant of this single-objective light-sheet microscope also permits applications that would otherwise not be feasible, including imaging cm-scale tissue preparations (**Supplementary Figure 10).**

As such, we believe that this single-objective light-sheet microscope could displace laser scanning and spinning-disk confocal microscopes as the workhorse of cell biology in both individual labs and user facilities. The single-objective design allows integration into existing epi-fluorescence frameworks, which decreases the cost of building such an instrument. Furthermore, it combines the spatial resolution of a high NA spinning disk microscope with high volumetric acquisition speed and low phototoxicity afforded by light-sheet microscopy. It provides comparable spatial resolution to Lattice Light-Sheet Microscopy, but with simpler sample handling, drastically reduced laser power requirements, and the ability to perform simultaneous multicolor imaging. And lastly, we have reported only on the highest resolution variant of single-objective light-sheet microscopes that incorporate the bespoke glass-tipped tertiary objective, and many different variants of the microscope that operate across a range of numerical apertures (1.0 – 1.35) and magnification (20 - 100X) have already been designed and numerically evaluated. Thus, we consider this the opening salvo in what may be the next generation of single-objective light-sheet microscopes.

Materials and Methods:

Laser Scanning Microscope Setup.

The entire microscope was built in a basic inverted geometry (RAMM-FULL, Applied Scientific Instrumentation) with a three-axis motorized stage controller. Two solid-state continuous wave lasers (Sapphire-488-200 and Sapphire-568-100, Coherent) and a continuous wave fiber laser (VFL-P-300-642-OEM1, MPB Communications) were independently attenuated with logarithmically spaced neutral density filter wheels, optically shuttered (VMM-D3, and LSS6T2, Uniblitz), and combined with dichroic mirrors (LM01-552-25 and LM01-613-25, Semrock). Much of this equipment was collected from a decommissioned OMX system, and future variants of the single-objective light-sheet microscope could include faster laser switching devices (e.g., solid state lasers or acousto-optic devices). After the laser combining dichroic mirrors, the beams were focused through a 30-micron pinhole (P30D, ThorLabs) with a 50 mm achromatic doublet (AC254-050-A, ThorLabs) and recollimated thereafter with a 100 mm achromatic doublet (AC254-100-A, ThorLabs). Laser polarization was controlled with a half waveplate (AHWP3, Bolder Vision Optik) that was secured in a rotation mount (RSP1X15, ThorLabs). The beam was then either reflected with a motorized flipper mirror (8892-K, Newport) towards the epi-illumination (for alignment) or laser spot (for optogenetics) path or transmitted towards the light-sheet illumination path.

For the light-sheet path (See **Supplementary Figures 3-5),** the light was first expanded in one dimension with a pair of cylindrical lenses (F=25mm, #68-160 Edmund Optics and ACY254-100-A, ThorLabs), and then focused into a 1D Gaussian profile using a cylindrical lens (ACY254-50-A, ThorLabs) onto a resonant galvo (CRS 12 kHz, Cambridge Technology) to reduce stripe artifacts. A 50mm focal length lens (AC254-50-A, ThorLabs) was used to Fourier transform the line profile, and an adjustable slit was placed in the Fourier plane (conjugate to primary objective pupil plane). This slit was used to adjust the effective NA of the light-sheet, which determines the light-sheet thickness and propagation length. For most experiments, the NA of the light-sheet was set to ~0.2, which creates a light-sheet with a Rayleigh length of about 21 microns. Opening the slit allows increasing the NA to 0.3, which is the practical limit for the chosen objective and inclination angle. The light was then relayed with 50 and 100 mm achromatic doublets (AC254-050-A, and AC254-100-A, ThorLabs) over a polarizing beam splitter (PBS251, ThorLabs), through a quarter wave plate (AQWP3, Bolder Vision Optik) onto mirror galvanometer (6215H, Cambridge Technology), which backreflects the light through the same quarter wave plate and polarizing beam splitter towards a multi-edge dichroic (Di03-R405/4888/561/635-t3-25x36, Semrock) that reflected the light towards the primary objective. The galvanometer mirror allows control of the lateral positioning of the light-sheet. After the dichroic, the light was focused with a 200 mm tube lens (TTL200, ThorLabs), recollimated with a 39 mm scan lens (LSM03-VIS, ThorLabs), reflected off of a 1D galvanometer mirror (6215H, Cambridge Technology), focused by a 70 mm scan lens (CSL-SL, ThorLabs), recollimated with a 200 mm tube lens (TTL200, ThorLabs), and imaged into the specimen with the primary objective (100X/1.35 MRD73950 Silicone Immersion Objective, Nikon Instruments). For detection (**Supplementary Figure 1**), the

fluorescence was descanned with the galvanometer mirror, transmitted through the multi-edge dichroic, and an image is formed by the secondary objective (CFI Plan Apo Lambda 40XC, Nikon Instruments), which is detected by the tertiary objective (AMS-AGY v1.0, Special Optics) and focused with a tube lens (ITL200, ThorLabs) onto a sCMOS camera (Flash 4.0 v3, Hamamatsu). Each imaging channel was collected sequentially (e.g., after a complete Z-stack), and the fluorescence was spectrally isolated with emission filters placed in a motorized filter wheel (FG-LB10-B and FG-LB10-NWE, Sutter Instruments). The scan galvanometer and resonant galvanometer were driven by a 28V (A28H1100M, Acopian) and a 12V power supply, respectively.

For widefield illumination, after being reflected by the flipper mirror, the light was focused onto a galvanometer mirror (6215H, Cambridge Technology) with an achromatic doublet (AC254-100-A, ThorLabs) that itself was mounted on a flipper mirror (8892-K, Newport). For laser spot illumination, the achromatic doublet was removed from the optical path, resulting in a collimated beam on the galvanometer mirror. Thereafter, the epi-illumination and laser spot illumination paths were reflected off the aforementioned polarizing beam splitter towards the multi-edge dichroic. The widefield illumination path proved useful for identifying interesting cells and for focusing the microscope, and the fluorescence was detected after the first tube lens with flipper-mounted dichroic mirror (Di02-R488-t3-25x36, Semrock) onto a sCMOS camera (Grasshopper 3, FLIR).

The data acquisition computer was a Colfax International ProEdge SXT9800 Workstation equipped with two Intel Xeon Silver 4112 processors operating at 2.6 GHz with 8 cores and 16 threads, 96 GB of 2.667 GHz DDR4 RAM, a Intel DC P3100 1024 GB M.2 NVMe drive, and a Micron 5200 ECO 7680 GB hard-drive for file storage. All software was developed using a 64-bit version of LabView 2016 equipped with the LabView Run-Time Engine, Vision Development Module, Vision Run-Time Module and all appropriate device drivers, including NI-RIO Drivers (National Instruments). Software communicated with the camera (Flash 4.0, Hamamatsu) via the DCAM-API for the Active Silicon Firebird frame-grabber and delivered a series of deterministic TTL triggers with a field programmable gate array (PCIe 7852R, National Instruments). These triggers included control of the optical shutters, galvanometer mirror scanning, camera fire and external trigger. Some of the core functions and routines in the microscope control software are licensed under an MTA from Howard Hughes Medical Institute, Janelia Research Campus. The control software can be requested from the corresponding authors and will be distributed under MTA with HHMI Janelia Research Campus.

Stage Scanning Microscope Setup.

The stage-scanning oblique plane microscope was built in a basic inverted geometry (RAMM, Applied Scientific Instrumentation) with a three-axis motorized stage controller and scan optimized X stage. Five solid-state continuous wave lasers (OBIS LX 405-100, OBIS LX 488-150, OBIS LS 561-150,

OBIS LX 637-140, and OBIS LX 730-30, Coherent Inc.) contained within a control box (Laser Box: OBIS, Coherent Inc.) were combined with dichroic mirrors (zt405rdc-UF1, zt488rdc-UF1, zt561rdc-UF1, zt640rdc-UF1, Chroma Technology Corporation). After the laser combining dichroic mirrors, the beams were focused through a 30-micron pinhole (P30D, Thorlabs) with a 30 mm achromatic doublet (AC254-030-A, Thorlabs) and recollimated thereafter with a 175 mm achromatic doublet (AC508-175-A, Thorlabs). Light was focused to a 1D Gaussian profile with achromatic cylindrical lens (ACY254-050-A, Thorlabs) with a variable slit (VA100C, Thorlabs) placed in the back focal plane of the cylindrical lens to control the numerical aperture of the light sheet. The line focus was formed on a mirror, used to control the light sheet tilt at the same plane, placed in the back focal plane of a 125 mm achromatic doublet (AC508-125-A). This lens was placed such that collimated light focused at the back focal plane of the primary objective (100X/1.35 MRD73950 Silicone Immersion Objective, Nikon Instruments). Excitation light was reflected off a pentaband dichroic mirror (zt405/488/561/640/730rpc-uf3, Chroma Technology Corporation) and imaged into the specimen with the primary objective.

For detection, fluorescence was transmitted through the pentaband dichroic mirror, reflected off a removable beam-turning mirror cube (DFM1-P01, Thorlabs), then transmitted through a 200 mm tube lens (MXA22018, Nikon Instruments), a 357 mm tube lens assembly (AC508-500-A and AC508-750-A, Thorlabs), and an image is formed by the secondary objective (CFI Plan Apo Lambda 40XC, Nikon Instruments), which is detected by the tertiary objective (AMS-AGY v1.0, Special Optics), passed through an empty kinematic mirror cube (DFM1-P01, Thorlabs) and focused with a tube lens (MXA22018, Nikon Instruments) onto a sCMOS camera (Prime BSI Express, Teledyne Photometrics). Each imaging channel was collected sequentially (e.g., after one complete strip scan of the stage), and laser light was blocked by two identical pentaband barrier filters (zet405/488/561/640/730m, Chroma Technology Corporation), with one placed in infinity space before secondary objective and one in infinity space after the tertiary objective. The kinematic mirror cubes after the primary and tertiary objectives are used to inject a 532 nm alignment laser (CPS532-C2, Thorlabs) and to redirect light to a wavefront sensor (HASO-VIS, Imagine Optic) to characterize the wavefront after the primary and tertiary objectives.

Acquisition was performed on a Windows 10 64-bit computer (Intel i7-5880K, 16 Gb memory, USB 3.0 12 TB SSD raid 0 array, Nvidia Titan X card). Data was acquired by scanning the scan optimized stage axis at a constant speed with the camera set to internal mode set and triggered to start when the stage passed the user defined “start” point. The scan speed was adjusted so that the displacement during any exposure is less than one pixel on the camera. This slow scan speed ensured that minimal motion artifacts occurred during stage scanning. The camera chip was cropped to the area of interest containing the sample and data was saved within one continuous TIFF file. Multiple laser lines are acquired sequentially by allowing the stage to reset to the original position and repeat the scan. A custom script in Micromanager 2.0 gamma sets the stage parameters and controls the scan. Code available at: http://www.github.com/QI2lab/OPM/tree/frozen-20200326.

Data Post-Processing.

For the laser-scanning system, analysis was performed on the local BioHPC high-performance computing cluster. Data was sheared with Python using a script originally developed by Dr. Bin Yang which applies the Fourier Shift Theorem. In instances where deconvolution was used, the raw data was deconvolved in a blind fashion where the experimentally measured PSF served as a prior. Both of these data post-processing functions are available via the AdvancedImagingUTSW GitHub repository (https://github.com/AdvancedImagingUTSW). For rotation into the traditional epi-fluorescence-like orientation, the freely available IMOD software package was used (Kremer et al., 1996).

For the stage-scanning system, analysis was performed on a Windows 10 64-bit computer (Intel i7-8700K, 128 Gb memory, 24 TB SNeSD raid 0 array, Nvidia Titan RTX card). Using Numpy and Dask libraries in Python (van der Walt et al., 2011), data was split into tiles that fit in local memory, orthogonally interpolated to deskew the stage scan (Maioli, 2017), saved as a BigDataViewer H5 file with GZIP compression (Pietzsch et al., 2015), [ref] and stitched using default settings in BigStitcher (Hörl et al., 2019). Data was further deskewed objective tilt in BigStitcher. Code available at: http://www.github.com/QI2lab/OPM/tree/frozen-20200326.

Cell lines, Plasmids and Transfection.

NK-92 cells were obtained from ATCC (CCL-2407) and maintained in alpha minimum modified Eagle medium, 0.2 mM myoinositol, 0.1 mM beta-mercaptoethanol, 0.02 mM folic acid, 12.5% heat inactivated horse serum, 12.5% heat-inactivated FBS (Sigma Aldrich), 2 mM L-glutamine and non-essential amino acids (ThermoFisher Scientific), supplemented with 100 U/mL Il-2 (Roche). K562 cells were obtained from ATCC (CCL-243) and cultivated in RPMI medium with high glucose, supplemented with 10% of heat-inactivated FBS (Sigma Aldrich), 2 mM L-glutamine and non-essential amino acids (ThermoFisher Scientific). Both NK-92 and K562 cells were maintained in 37°C, 5% CO_2 tissue culture incubators and routinely confirmed to be mycoplasma negative using LookOut mycoplasma PCR detection kit (Sigma Aldrich). pLifeAct-mScarlet-N1 and pLck-mVenus-C1 were gifts from Dorus Gadella (Addgene plasmids #85054 and #84337) and transfected by nucleofection using Amaxa Kit R per manufacturer's instructions (Lonza). Positive cells were amplified under antibiotic selection pressure and sorted for low or intermediate expression level of the fluorescently tagged protein on an Aria II Fluorescence Activated Cell Sorter (BD). Each sorted population was then used for pilot experiments to determine the lowest possible expression level required for optimal imaging conditions. NK-92 cells expressing Life-Act-mScarlet and K562 cells expressing Lck-mVenus were mixed 1:1 and briefly spun down and resuspended in full prewarmed medium. The cell conjugates were then seeded in #1.5 uncoated glass bottom dishes and imaged as soon as

possible for up to 45 minutes post mixing. All imaging was performed at 37°C using pre-warmed media and a stage top insert enclosing the sample.

Long-term estrogen deprived (LTED) MCF7 cell lines have been described previously (Miller et al., 2010). To generate stably transduced cell lines, 1 μg of pEGFP-AKT-PH plasmids were co-transfected with 0.75 μg of psPAX2 (2nd generation lentiviral packaging plasmid) and 0.5 μg of pMD2.G (VSV-G envelope expressing plasmid) into 293FT cells using Lipofectamine2000 (ThermoFisher). Cell medium was changed to fresh medium 24 h post-transfection, and then were collected 48 h later. Virus-containing medium was applied to target cells with 8 μg/mL polybrene. After 72 h from the infection, cells were sorted for GFP expression by flow cytometry.

To stably express EGFP-Sec61b in U2OS cells, a TET-inducible EGFP-Sec61b fusion was knocked into the AAVS1 (Qian et al., 2014) safe harbor locus. The homologous recombination donor (HRD) was generated by inserting an EGFP tag and Sec61b cDNA (mEmerald-Sec61b-C1 (Nixon-Abell et al., 2016) was a gift from Dr. Jennifer Lippincott-Schwartz, Addgene #90992) amplified with EGFP-F, EGFP-R, Sec61b-F, and Sec61b-R primers (see Supplementary Table 2), cloned into the AAVS1-TRE3G-EGFP vector (AAVS1-TRE3G-EGFP was a gift from Su-Chun Zhang, Addgene #52343), and linearized with MluI and SalI using Gibson assembly. U2OS cells were cultured in RPMI (Gibco, A4192301) media supplemented with 10% FBS and Pen/Strep at 37 °C, 5% CO2. For AAVS1 locus knock-in, 1 µg of HRD plasmid and 1 µg of AAVS1 T2 CRISPR plasmid (AAVS1 T2 CRISPR in pX330 (Natsume et al., 2016) was a gift from Masato Kanemaki, Addgene plasmid #72833) were transfected into U2OS cells using FuGENE HD (Promega) according to the manufacturer's instructions. 48 hours after transfection selection was initiated with 1 µg/ml of puromycin. The FBS used was not tetracycline free, sufficient EGFP-Sec61b expression was achieved without the addition of doxycycline.

The human melanoma cell line1205Lu (a gift from Dr. Meenhard Herlyn, Wistar Institute) was genotypically characterized as previously reported (Smalley et al., 2007a; Smalley et al., 2007b) and grown in high glucose DMEM (11965092, Gibco, Thermo Fisher Scientific) supplemented with 10% fetal bovine serum (10100147, Gibco, Thermo Fisher Scientific), 1x Mem Non-essential amino acids (11140050, Gibco, Thermo Fisher Scientific) and 50 U/ml penicillin/ 50 µg/ml streptomycin (15070063, Gibco, Thermo Fisher Scientific). pLenti CMV Hygro 3xnls-mScarlet-I was generated by Gateway Gene Cloning (Invtirogen, Thermo Fisher Scientific). First, 3xnls-mScarlet-I (a gift from Dr. Dorus Gadella (Addgene #98816 (Bindels et al., 2016; Chertkova et al., 2020) was amplified by PCR (M0515, Q5 Hot start, New England Biolabs) to introduce 5' EcoRI and 3' XbaI restriction enzyme sites flanking either ends of 3xnls mScarlet-I sequence (5' EcoRI and 3' XbaI primer). The entry vector pENTR1A-GFP-N2 (FR1) (a gift from Dr. Eric Campeau & Dr. Paul Kaufman (Addgene #19364) along with the purified PCR fragment was digested with EcoRI and XbaI then ligated together with T4 DNA ligase (M0202, New England Biolabs). pENTR1a-3xnls-mScarlet-I was then recombined using Gateway LR Clonase II (11791, Invitrogen, Thermo Fisher Scientific) as per the manufacturer's instructions into pLenti CMV Hygro DEST (W117-1) (a gift from Dr. Eric Campeau & Dr. Paul Kaufman (Addgene #17454) to create the final vector which was sequence verified by Sanger

sequencing (Australian Genome Research Facility). CRISPR-CAS9 Endogenous meGFP tagging of the TUB1AB genetic locus in 1205Lu cells was performed as previously described (Khan et al., 2017) with the following modifications. Cells were transfected with 3.5 µg of each CAS-9-guide and eGFP donor knock-in vector using Lipofectamine 2000 (11668019, Invitrogen, Thermo Fisher Scientific) for 6 hours before replacing media to allow cells to recover. To achieve a uniformly fluorescent population of cells, cells were sorted using a MoFlo Astrios EQ cell sorter (Beckman Coulter) to isolate cells with dual-positive expression profile of meGFP and mScarlet-I using a gating strategy isolating the top ~20% of meGFP and an intermediate ~30%-60% population of mScarlet-I. To label the nucleus, 1205Lu cells were lentivirally transduced to stably overexpress 3xnls-mScarlet-I as previously published (Coleman et al., 2003). After successful transduction, cells were grown in media containing 0.1 mg/ml Hygromycin (H3274, Roche).

Cardiomyocytes were isolated from the left ventricle of 1- to 2-day-old Sprague-Dawley rats. The isolation process and initial culture was described previously (Morales et al., 2016). Cells seeded on a 35mm plate were stained with Fluo-3 AM calcium indicator (Thermofisher) at 1 μM for 20 minutes incubation after which seeded cells were image on the microscope using 488nm excitation.

MV3 cells were obtained from Peter Friedl (MD Anderson Cancer Center, Houston TX). MV3 cells were cultured in DMEM (Gibco) supplemented with 10% fetal bovine serum (FBS; ThermoFisher) in 37°C and 5% CO_2. MV3 cells expressing photoactivatable PI3K and Akt-PH sensor were used post infection with a lentiviral constructs expressing cytosolic (cry2) and membrane-targeting (CAAX) domain such that light activation of PI3K occurs through hetrodimerization. The pLVX-mRuby2-iSH2 construct was made by replacing mCherry with mRuby2 in mCherry-cry2-iSH2 contruct (Addgene Plasmid #66839) (Idevall-Hagren et al., 2012) and cloned into pLVX-puro vector (Clontech). Similarly, the CIBN-CAAX plasmid was obtained from Addgene (Plasmid #79574) and cloned into pLVX-neo vector (Clontech). Lentivirus was produced and cells were infected according to the manufacturer's instructions (Clontech). Cells were selected for expression via puromycin and neomycin (Thermofisher). Cells were then also infected with Akt-PH-SNAP construct and flow sorted (BD FACS Aria) for higher expressing cells. MV3 expressing genetically encoded multimeric nanoparticles (GEMs) were made by infection with lentiviral construct from Addgene (Plasmid #116934) (Delarue et al., 2018). Cells were FACS sorted to purify a population of cells expressing GEMs. The membrane marker expressed in MV3 cells was created from the membrane targeting (i.e. CAAX) domain of KRas fused to the HALO tag and cloned into the pLVX vector. Cells were infected with virus containing this construct and selected for expression by G418 resistance.

Imaging and photoactivation of PI3K was done on cells plated on 35 mm dish with cover glass (P35G-1.5-14-C, Mattek) coated with 10 mg/mL fibronectin. Prior to imaging in optogenetics experiments, cells were stained with snap tag SNAP-Cell 647-SiR (S9136S, New England Biolab Inc.). Activation was done with the point scanning defined 2D rectangle using a 488 nm laser for the duration of the activation period at 0.1 Hz (beam diameter ~1.49 µm2, laser intensity ~2 kW/cm^2). Before imaging CAAX-Halo MV3 cells were incubated with 1 μM of HALO tag (HALO-Tag Oregon Green ligand, Promega #G2801) and

imaged using 488nm laser at 0.93 Hz. ARPE and RPE hTERT cells were generated and cultured as previously described (Aguet et al., 2013; Gan et al., 2016).

Microfluidic Printing, Fabrication, and Casting.

Masks were designed using Tanner L-edit IC Layout (Mentor, Siemens Business) and printed using a Heidelberg µPG 101 mask writer (Heidelberg instruments) to create a 5-inch square chrome photomask on a soda lime glass substrate. After photomask printing, photomasks were developed in AZ 726 MIF developer (MicroChemicals), etched in chromium etchant (651826, Sigma Aldrich) and cleaned in an ultrasonic acetone bath (V800023, Sigma Aldrich). To create master molds, 4-inch round silicon wafers were surface etched with hydrofluoric acid (339261, Sigma-Aldrich) to remove the surface silicone oxide layer in order to ensure photoresist adhesion to the underlying silicon wafer. Master mold of approximately 5 µm height were created using manufacturers recommended spin coating and post-spin coating processing guidelines for SU-8 2005 negative photoresist (MicoChemicals). SU-8 2005 spin coated silicon wafers were contact printed using the developed photomasks on an EVG620 mask aligner (Ev Group) with 360 nm light exposure at a dose of 120 mJ/cm^2 and post-baked according to manufacturer recommended guidelines (MicroChemicals). Prior to the first casting, each master mold was vapor deposition silanized with Trichloro (1H, 1H, 2H, 2H-perfluorooctyl) silane (448931, Sigma-Aldrich) in a vacuum desiccator (Scienceware, Sigma-Aldrich) to create an anti-stiction layer for PDMS demolding as previously described (Qin et al., 2010). To create micro channels, Polydimethylsiloxane elastomer (PDMS) castings of the master mold were made using SYLGARD 184 silicone elastomer (Dow Corning) and prepared and cured according to manufacturer's recommended instructions. PDMS microchannels were cut to size using a razor blade before cell seeding ports were created using a 3.0 mm diameter biopsy punch (ProSciTech) at opposite ends of a 1500 µm length microchannel array. PDMS microchannel were bonded to glass bottom dishes (P35G-1.0-14-C, Mattek) using a corona tool (Electro-Technic Products Inc.) as previously published (Haubert et al., 2006), sterilized with 100% ethanol before being incubated overnight with 20 µg/ml bovine telo-collagen I in PBS (5225, Advanced Biomatrix). On the day of assay, each dish was replaced with fully complemented media before seeding cells into each of the seeding ports.

Silanization of Coverslips

To promote covalent adhesion of tissue and polyacrylamide gel to glass coverslips, coverslips were silanized according to previously published methods (Moffitt, OCT 2016). In short, 40mm, #1.5 coverslips (0420-0323-2, Bioptechs) were washed at room temperature in solution consisting of 1:1 (vol/vol) 37% HCl and Methanol for 30 min, rinsed in DI water three times and then dried at 60-70°C. Following this, coverslips were washed in solution consisting of chloroform with 0.1% (vol/vol) triethylamine (TX1200, Millipore) and 0.2% (vol/vol) allyltrichlorosilane (107778, Sigma) for 30 minutes at room temperature. Finally, coverslips were washed once in chloroform and once in ethanol and then baked for 1 hour at 60-70°C. Coverslips were then stored in a vacuum desiccation chamber before use.

Tissue Preparation

Mouse brain tissue was procured, cleared with ice cold, nuclease-free 1x PBS solution and fixed with ice-cold 4%, nuclease-free PFA solution via transcardial perfusion. Following fixation, brain tissue was dissected and post-fixed for overnight at 4°C. Tissue was then cryo-preserved in 15% then 30% nuclease-free sucrose solution before freezing in OCT and cut into 40μM coronal sections via vibratome. Sections were stored in nuclease-free, 1x PBS solution at 4°C prior to mounting and staining.

Tissue Staining

Tissue staining, embedding and digestion protocols were derived from previously published protocols with some adaptation (Moffitt, OCT 2016). Prepared tissue sections were mounted to 40mm silanized coverslips and dried for 15 min at 37°C to securely affix tissue to the coverslip. To permeabilize tissue, coverslip mounted samples were immersed in 70% ethanol solution overnight at 4°C. Samples were then immersed in formamide wash buffer consisting of 2x saline-sodium citrate (SSC; ThermoFisher, AM9763) with 30% (vol/vol) formamide (AM9342, ThermoFisher) for 30 min at 37°C followed staining with probes in 200μL hybridization buffer consisting of 2x SSC, 30% (vol/vol) formamide, 0.1 % (wt/vol) yeast tRNA (15401011, Life Technologies Corp), 1% (vol/vol) murine RNase inhibitor (M0314L, New England Biolabs) and 10% (wt/vol) dextran sulfate (D8906, Sigma) for 24 hours at 37°C in a humidified chamber consisting of a square polystyrene bioassay dish with a wet paper towel folded and lining the chamber and film-sealed. Hybridization buffer with probes and linker were pipetted onto the surface of a glass plate and the coverslip-mounted sample was carefully inverted onto the buffer. GAPDH (SMF-3140-1, BioSearch Technologies) and POLR2A probes (VSMF-3060-5, BioSearch Technologies) were used at a concentration of 2.5μM each and an additional anchor probe, designed to link the poly-adenylated tails of RNA to the polyacrylamide gel matrix, was added to the hybridization buffer at a concentration of 1μM to cross-link RNA to the acrylamide gel matrix. Following hybridization, samples were immersed in formamide wash buffer for 30 min at 37°C to rinse away any unbound probe.

Gel Embedding and Clearing of Tissue

To improve the optical clarity of the tissue samples, we removed light scattering proteins and lipids. To achieve this, the samples were first embedded to a polyacrylamide gel matrix and then enzymatically digested to remove proteins and chemically dissolved to remove lipids as previously described (Moffitt OCT 2016). In short, samples were washed for two minutes with degassed polyacrylamide (PA) solution consisting of 4% (vol/vol) 19:1 acrylamide/bis-acrylamide (161010144, BioRad), 60 mM Tris-HCl pH 8 (AM9856, ThermoFisher), and 0.3 M NaCl (AM9759, Thermofisher) and then washed for two minutes with PA gel solution which consists of PA solution with the addition of polymerizing agents TEMED (Sigma, T9281) and ammonium persulfate (A3678, Sigma). The PA gel solution was then aspirated from the

coverslip-mounted sample. To cast the gel film, 200μL PA gel solution was applied to the surface of a Gel Slick (50640, Lonza) coated glass plate and the coverslip-mounted sample was inverted onto the PA Gel solution, creating a thin layer of gel solution between the two panes of glass. The PA gel was allowed to cast for 1.5 hour. Coverslip and affixed gel film were carefully removed from the glass plate. Following the gel embedding, samples were washed twice for 5 min with digestion buffer consisting of nuclease-free water with 0.8 M guanidine-HCl (G3272, Sigma), 50 mM Tris-HCl pH 8, 1 mM EDTA and 0.5% (vol/vol) Triton X-100 (T8787, Sigma). Once complete, samples were incubated in digestion enzyme buffer consisting of digestion buffer supplemented with (0.5%) proteinase K (P8107S, New England Biolabs) and 5% Pronase (11459643001, Sigma), at a concentration of 80 U/mL, at 37°C for 24 hours to clear the tissue. Once cleared, tissue was washed in 2x SSC buffer three times for 5 min. After clearing, tissue was stained with DAPI at a concentration of 50ug/mL in 2x SSC buffer overnight at 37°C. Sample was then washed in 2x SSC buffer two times for 5 min and mounted to a glass plate using ProLong™ Glass Antifade Mountant (P36982, ThermoFisher).

Acknowledgements:

The authors would like to thank the Cancer Prevention Research Institute of Texas (RR160057, to R.F.) and UT Southwestern Medical Center for their generous funding, and the lab of Professor Joseph Hill for providing primary cardiomyocytes for calcium imaging. A.B.H. receives research grant support from Takeda. C.L.A. receives or has received research grants from Puma Biotechnology, Pfizer, Lilly, Bayer, Takeda, and Radius; holds stock options in Provista and Y-TRAP; serves or has served in an advisory role to Novartis, Merck, Lilly, Symphogen, Daiichi Sankyo, Radius, Taiho Oncology, H3Biomedicine, OrigiMed, Puma Biotechnology, and Sanofi; and reports scientific advisory board renumeration from the Komen Foundation. This work was supported by grants from the NIH (R00 FM120386 to J.C.S., R01HL068702 to D.P.S., R33CA235254 and R35GM133522 to R.F.). J.C.S. is a Damon Runyon Dale F. Frey Scientist supported (in part) by the Damon Runyon Cancer Research Foundation (DFS-24-17), and D.P.S. is a member of the Chan Zuckerberg Initiative Seed Network Human Lung Cell Atlas v1.0.

Competing interests:

K.M.D. and R.F. have an investment interest in Discovery Imaging Systems, LLC. C.L.A. serves in an advisory role for Novartis, which has an investment interest in alpelisib. There are no other competing interests.

References:

Aguet, F., Antonescu, Costin N., Mettlen, M., Schmid, Sandra L., and Danuser, G. (2013). Advances in Analysis of Low Signal-to-Noise Images Link Dynamin and AP2 to the Functions of an Endocytic Checkpoint. Developmental Cell *26*, 279-291. 10.1016/j.devcel.2013.06.019

Andre, F., Ciruelos, E., Rubovszky, G., Campone, M., Loibl, S., Rugo, H.S., Iwata, H., Conte, P., Mayer, I.A., Kaufman, B.*, et al.* (2019). Alpelisib for PIK3CA-Mutated, Hormone Receptor-Positive Advanced Breast Cancer. N Engl J Med *380*, 1929-1940. 10.1056/NEJMoa1813904

Asthagiri, A.R., Ma, X., Dagliyan, O., Hahn, K.M., and Danuser, G. (2018). Profiling cellular morphodynamics by spatiotemporal spectrum decomposition. PLOS Computational Biology *14*. 10.1371/journal.pcbi.1006321

Bindels, D.S., Haarbosch, L., van Weeren, L., Postma, M., Wiese, K.E., Mastop, M., Aumonier, S., Gotthard, G., Royant, A., Hink, M.A.*, et al.* (2016). mScarlet: a bright monomeric red fluorescent protein for cellular imaging. Nature Methods *14*, 53-56. 10.1038/nmeth.4074

Botcherby, E.J., Smith, C.W., Kohl, M.M., Debarre, D., Booth, M.J., Juskaitis, R., Paulsen, O., and Wilson, T. (2012). Aberration-free three-dimensional multiphoton imaging of neuronal activity at kHz rates. Proceedings of the National Academy of Sciences *109*, 2919-2924. 10.1073/pnas.1111662109

Bouchard, M.B., Voleti, V., Mendes, C.S., Lacefield, C., Grueber, W.B., Mann, R.S., Bruno, R.M., and Hillman, E.M.C. (2015). Swept confocally-aligned planar excitation (SCAPE) microscopy for high-speed volumetric imaging of behaving organisms. Nature Photonics *9*, 113-119. 10.1038/nphoton.2014.323

Carisey, A.F., Mace, E.M., Saeed, M.B., Davis, D.M., and Orange, J.S. (2018). Nanoscale Dynamism of Actin Enables Secretory Function in Cytolytic Cells. Current Biology *28*, 489-502.e489. 10.1016/j.cub.2017.12.044

Chakraborty, T., Driscoll, M.K., Jeffery, E., Murphy, M.M., Roudot, P., Chang, B.-J., Vora, S., Wong, W.M., Nielson, C.D., Zhang, H.*, et al.* (2019). Light-sheet microscopy of cleared tissues with isotropic, subcellular resolution. Nature Methods *16*, 1109-1113. 10.1038/s41592-019-0615-4

Chen, B.-C., Legant, W.R., Wang, K., Shao, L., Milkie, D.E., Davidson, M.W., Janetopoulos, C., Wu, X.S., Hammer, J.A., Liu, Z.*, et al.* (2014). Lattice light-sheet microscopy: Imaging molecules to embryos at high spatiotemporal resolution. Science *346*. 10.1126/science.1257998

Chertkova, A.O., Mastop, M., Postma, M., van Bommel, N., van der Niet, S., Batenburg, K.L., Joosen, L., Gadella, T.W.J., Okada, Y., and Goedhart, J. (2020). 10.1101/160374

Chhetri, R.K., Amat, F., Wan, Y., Höckendorf, B., Lemon, W.C., and Keller, P.J. (2015). Whole-animal functional and developmental imaging with isotropic spatial resolution. Nature Methods *12*, 1171-1178. 10.1038/nmeth.3632

Coleman, J.E., Huentelman, M.J., Kasparov, S., Metcalfe, B.L., Paton, J.F.R., Katovich, M.J., Semple-Rowland, S.L., and Raizada, M.K. (2003). Efficient large-scale production and concentration of HIV-1-based lentiviral vectors for use in vivo. Physiological Genomics *12*, 221-228. 10.1152/physiolgenomics.00135.2002

Dean, K.M., Roudot, P., Welf, E.S., Pohlkamp, T., Garrelts, G., Herz, J., and Fiolka, R. (2017). Imaging subcellular dynamics with fast and light-efficient volumetrically parallelized microscopy. Optica *4*. 10.1364/optica.4.000263

Delarue, M., Brittingham, G.P., Pfeffer, S., Surovtsev, I.V., Pinglay, S., Kennedy, K.J., Schaffer, M., Gutierrez, J.I., Sang, D., Poterewicz, G.*, et al.* (2018). mTORC1 Controls Phase Separation and the Biophysical Properties of the Cytoplasm by Tuning Crowding. Cell *174*, 338-349.e320. 10.1016/j.cell.2018.05.042

Denais, C.M., Gilbert, R.M., Isermann, P., McGregor, A.L., te Lindert, M., Weigelin, B., Davidson, P.M., Friedl, P., Wolf, K., and Lammerding, J. (2016). Nuclear envelope rupture and repair during cancer cell migration. Science *352*, 353-358. 10.1126/science.aad7297

Dunsby, C. (2008). Optically sectioned imaging by oblique plane microscopy. Optics Express *16*. 10.1364/oe.16.020306

Gan, Z., Ding, L., Burckhardt, Christoph J., Lowery, J., Zaritsky, A., Sitterley, K., Mota, A., Costigliola, N., Starker, Colby G., Voytas, Daniel F.*, et al.* (2016). Vimentin Intermediate Filaments

Template Microtubule Networks to Enhance Persistence in Cell Polarity and Directed Migration. Cell Systems *3*, 252-263.e258. 10.1016/j.cels.2016.08.007

Garcia-Arcos, J.M., Chabrier, R., Deygas, M., Nader, G., Barbier, L., Sáez, P.J., Mathur, A., Vargas, P., and Piel, M. (2019). Reconstitution of cell migration at a glance. Journal of Cell Science *132*. 10.1242/jcs.225565

Gilbert, G., Demydenko, K., Dries, E., Puertas, R.D., Jin, X., Sipido, K., and Roderick, H.L. (2020). Calcium Signaling in Cardiomyocyte Function. Cold Spring Harbor Perspectives in Biology *12*. 10.1101/cshperspect.a035428

Hannezo, E., and Heisenberg, C.-P. (2019). Mechanochemical Feedback Loops in Development and Disease. Cell *178*, 12-25. 10.1016/j.cell.2019.05.052

Haubert, K., Drier, T., and Beebe, D. (2006). PDMS bonding by means of a portable, low-cost corona system. Lab on a Chip *6*. 10.1039/b610567j

Hörl, D., Rojas Rusak, F., Preusser, F., Tillberg, P., Randel, N., Chhetri, R.K., Cardona, A., Keller, P.J., Harz, H., Leonhardt, H.*, et al.* (2019). BigStitcher: reconstructing high-resolution image datasets of cleared and expanded samples. Nature Methods *16*, 870-874. 10.1101/343954

Huisken, J. (2004). Optical Sectioning Deep Inside Live Embryos by Selective Plane Illumination Microscopy. Science *305*, 1007-1009. 10.1126/science.1100035

Huisken, J., and Stainier, D.Y.R. (2007). Even fluorescence excitation by multidirectional selective plane illumination microscopy (mSPIM). Optics Letters *32*. 10.1364/ol.32.002608

Idevall-Hagren, O., Dickson, E.J., Hille, B., Toomre, D.K., and De Camilli, P. (2012). Optogenetic control of phosphoinositide metabolism. Proceedings of the National Academy of Sciences *109*, E2316-E2323. 10.1073/pnas.1211305109

Jaqaman, K., Loerke, D., Mettlen, M., Kuwata, H., Grinstein, S., Schmid, S.L., and Danuser, G. (2008). Robust single-particle tracking in live-cell time-lapse sequences. Nature Methods *5*, 695-702. 10.1038/nmeth.1237

Keller, P.J., Pampaloni, F., and Stelzer, E.H.K. (2007). Three-dimensional preparation and imaging reveal intrinsic microtubule properties. Nature Methods *4*, 843-846. 10.1038/nmeth1087

Keller, P.J., Schmidt, A.D., Wittbrodt, J., and Stelzer, E.H.K. (2008). Reconstruction of Zebrafish Early Embryonic Development by Scanned Light Sheet Microscopy. Science *322*, 1065-1069. 10.1126/science.1162493

Khan, A.O., Simms, V.A., Pike, J.A., Thomas, S.G., and Morgan, N.V. (2017). CRISPR-Cas9 Mediated Labelling Allows for Single Molecule Imaging and Resolution. Scientific Reports *7*. 10.1038/s41598-017-08493-x

Kremer, J.R., Mastronarde, D.N., and McIntosh, J.R. (1996). Computer Visualization of Three-Dimensional Image Data Using IMOD. Journal of Structural Biology *116*, 71-76. 10.1006/jsbi.1996.0013

Kumar, M., Kishore, S., Nasenbeny, J., McLean, D.L., and Kozorovitskiy, Y. (2018). Integrated one- and two-photon scanned oblique plane illumination (SOPi) microscopy for rapid volumetric imaging. Optics Express *26*. 10.1364/oe.26.013027

Kumar, S., Wilding, D., Sikkel, M.B., Lyon, A.R., MacLeod, K.T., and Dunsby, C. (2011). High-speed 2D and 3D fluorescence microscopy of cardiac myocytes. Optics Express *19*. 10.1364/oe.19.013839

Kumari, S., Mak, M., Poh, Y.C., Tohme, M., Watson, N., Melo, M., Janssen, E., Dustin, M., Geha, R., and Irvine, D.J. (2020). Cytoskeletal tension actively sustains the migratory T-cell synaptic contact. The EMBO Journal *39*. 10.15252/embj.2019102783

Li, D., Shao, L., Chen, B.C., Zhang, X., Zhang, M., Moses, B., Milkie, D.E., Beach, J.R., Hammer, J.A., Pasham, M.*, et al.* (2015). Extended-resolution structured illumination imaging of endocytic and cytoskeletal dynamics. Science *349*, aab3500-aab3500. 10.1126/science.aab3500

Mace, E.M., Dongre, P., Hsu, H.-T., Sinha, P., James, A.M., Mann, S.S., Forbes, L.R., Watkin, L.B., and Orange, J.S. (2014). Cell biological steps and checkpoints in accessing NK cell cytotoxicity. Immunology and Cell Biology *92*, 245-255. 10.1038/icb.2013.96

Mace, E.M., and Orange, J.S. (2014). Lytic immune synapse function requires filamentous actin deconstruction by Coronin 1A. Proceedings of the National Academy of Sciences *111*, 6708-6713. 10.1073/pnas.1314975111

Maioli, V.A. (2017). High-speed 3-D fluorescence imaging by oblique plane microscopy: multi-well plate-reader development, biological applications and image analysis (PhD thesis). 10.25560/68022

Marrack, P., Brown, A.C.N., Oddos, S., Dobbie, I.M., Alakoskela, J.-M., Parton, R.M., Eissmann, P., Neil, M.A.A., Dunsby, C., French, P.M.W.*, et al.* (2011). Remodelling of Cortical Actin Where Lytic Granules Dock at Natural Killer Cell Immune Synapses Revealed by Super-Resolution Microscopy. PLoS Biology *9*. 10.1371/journal.pbio.1001152

Miller, T.W., Hennessy, B.T., Gonzalez-Angulo, A.M., Fox, E.M., Mills, G.B., Chen, H., Higham, C., Garcia-Echeverria, C., Shyr, Y., and Arteaga, C.L. (2010). Hyperactivation of phosphatidylinositol-3 kinase promotes escape from hormone dependence in estrogen receptor-positive human breast cancer. J Clin Invest *120*, 2406-2413. 10.1172/JCI41680

Millett-Sikking, A., Dean, K.M., Fiolka, R., Fardad, A., Whitehead, L., and York, A. (2019). High NA single-objective light-sheet. Zenodo. 10.5281/zenodo.3244420

Miner, C.A., Giri, T.K., Meyer, C.E., Shabsovich, M., and Tripathy, S.K. (2015). Acquisition of Activation Receptor Ligand by Trogocytosis Renders NK Cells Hyporesponsive. The Journal of Immunology *194*, 1945-1953. 10.4049/jimmunol.1402408

Morales, C.R., Li, D.L., Pedrozo, Z., May, H.I., Jiang, N., Kyrychenko, V., Cho, G.W., Kim, S.Y., Wang, Z.V., Rotter, D.*, et al.* (2016). Inhibition of class I histone deacetylases blunts cardiac hypertrophy through TSC2-dependent mTOR repression. Science Signaling *9*, ra34-ra34. 10.1126/scisignal.aad5736

Natsume, T., Kiyomitsu, T., Saga, Y., and Kanemaki, M.T. (2016). Rapid Protein Depletion in Human Cells by Auxin-Inducible Degron Tagging with Short Homology Donors. Cell Rep *15*, 210-218. 10.1016/j.celrep.2016.03.001

Nixon-Abell, J., Obara, C.J., Weigel, A.V., Li, D., Legant, W.R., Xu, C.S., Pasolli, H.A., Harvey, K., Hess, H.F., Betzig, E.*, et al.* (2016). Increased spatiotemporal resolution reveals highly dynamic dense tubular matrices in the peripheral ER. Science *354*. 10.1126/science.aaf3928

Pietzsch, T., Saalfeld, S., Preibisch, S., and Tomancak, P. (2015). BigDataViewer: visualization and processing for large image data sets. Nature Methods *12*, 481-483. 10.1038/nmeth.3392

Qian, K., Huang, C.T., Chen, H., Blackbourn, L.W.t., Chen, Y., Cao, J., Yao, L., Sauvey, C., Du, Z., and Zhang, S.C. (2014). A simple and efficient system for regulating gene expression in human pluripotent stem cells and derivatives. Stem Cells *32*, 1230-1238. 10.1002/stem.1653

Qin, D., Xia, Y., and Whitesides, G.M. (2010). Soft lithography for micro- and nanoscale patterning. Nature Protocols *5*, 491-502. 10.1038/nprot.2009.234

Raab, M., Gentili, M., de Belly, H., Thiam, H.R., Vargas, P., Jimenez, A.J., Lautenschlaeger, F., Voituriez, R., Lennon-Dumenil, A.M., Manel, N.*, et al.* (2016). ESCRT III repairs nuclear envelope ruptures during cell migration to limit DNA damage and cell death. Science *352*, 359-362. 10.1126/science.aad7611

Ritter, Alex T., Asano, Y., Stinchcombe, Jane C., Dieckmann, N.M.G., Chen, B.-C., Gawden-Bone, C., van Engelenburg, S., Legant, W., Gao, L., Davidson, Michael W.*, et al.* (2015). Actin Depletion Initiates Events Leading to Granule Secretion at the Immunological Synapse. Immunity *42*, 864-876. 10.1016/j.immuni.2015.04.013

Smalley, K.S.M., Contractor, R., Haass, N.K., Kulp, A.N., Atilla-Gokcumen, G.E., Williams, D.S., Bregman, H., Flaherty, K.T., Soengas, M.S., Meggers, E.*, et al.* (2007a). An Organometallic Protein Kinase Inhibitor Pharmacologically Activates p53 and Induces Apoptosis in Human Melanoma Cells. Cancer Research *67*, 209-217. 10.1158/0008-5472.Can-06-1538

Smalley, K.S.M., Contractor, R., Haass, N.K., Lee, J.T., Nathanson, K.L., Medina, C.A., Flaherty, K.T., and Herlyn, M. (2007b). Ki67 expression levels are a better marker of reduced melanoma growth following MEK inhibitor treatment than phospho-ERK levels. British Journal of Cancer *96*, 445-449. 10.1038/sj.bjc.6603596

van der Walt, S., Colbert, S.C., and Varoquaux, G. (2011). The NumPy Array: A Structure for Efficient Numerical Computation. Computing in Science & Engineering *13*, 22-30. 10.1109/mcse.2011.37

Voigt, F.F., Kirschenbaum, D., Platonova, E., Pagès, S., Campbell, R.A.A., Kastli, R., Schaettin, M., Egolf, L., van der Bourg, A., Bethge, P.*, et al.* (2019). The mesoSPIM initiative: open-source light-sheet microscopes for imaging cleared tissue. Nature Methods. 10.1038/s41592-019-0554-0

Voleti, V., Patel, K.B., Li, W., Perez Campos, C., Bharadwaj, S., Yu, H., Ford, C., Casper, M.J., Yan, R.W., Liang, W.*, et al.* (2019). Real-time volumetric microscopy of in vivo dynamics and large-scale samples with SCAPE 2.0. Nature Methods *16*, 1054-1062. 10.1038/s41592-019-0579-4

Welf, E.S., Ahmed, S., Johnson, H.E., Melvin, A.T., and Haugh, J.M. (2012). Migrating fibroblasts reorient directionality by a metastable, PI3K-dependent mechanism. The Journal of Cell Biology *197*, 105-114. 10.1083/jcb.201108152

Wolf, K., te Lindert, M., Krause, M., Alexander, S., te Riet, J., Willis, A.L., Hoffman, R.M., Figdor, C.G., Weiss, S.J., and Friedl, P. (2013). Physical limits of cell migration: Control by ECM space and nuclear deformation and tuning by proteolysis and traction force. The Journal of Cell Biology *201*, 1069-1084. 10.1083/jcb.201210152

Yang, B., Chen, X., Wang, Y., Feng, S., Pessino, V., Stuurman, N., Cho, N.H., Cheng, K.W., Lord, S.J., Xu, L.*, et al.* (2019). Epi-illumination SPIM for volumetric imaging with high spatial-temporal resolution. Nature Methods *16*, 501-504. 10.1038/s41592-019-0401-3

Supplementary Figures

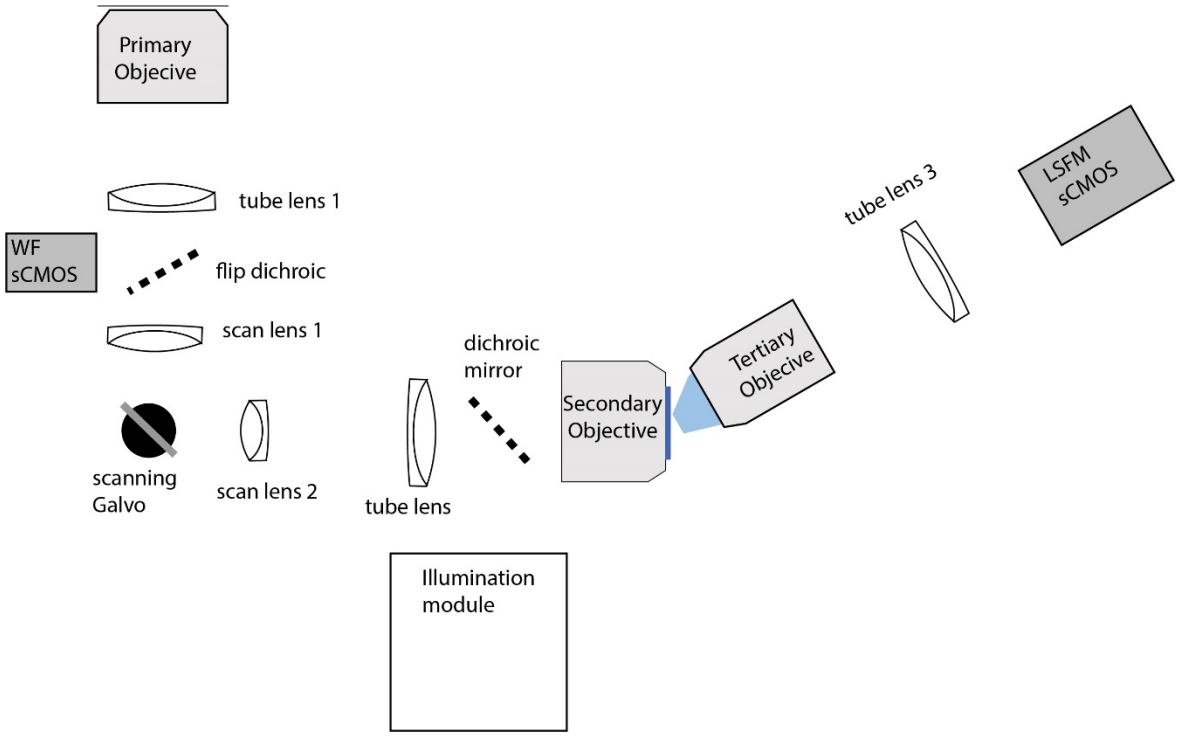

Supplementary Figure 1. Schematic diagram of the microscope. Primary objective: 100X/1.35 MRD73950 Silicone Immersion Objective, Nikon Instruments; tube lens 1: TTL200, ThorLabs; WF sCMOS: Grasshopper 3, FLIR; scan lens 1: CSL-SL, ThorLabs; scanning galvo: 6215H, Cambridge Technology; scan lens 2: LSM03-VIS, ThorLabs; tube lens 2: TTL200; Secondary objective: CFI Plan Apo Lambda 40XC, Nikon Instruments; tertiary objective: AMS-AGY v1.0, Special Optics; tube lens 3: ITL200 Thorlabs; LSFM sCMOS: Flash 4.0 v3, Hamamatsu. The illumination module is detailed in **Supplementary Figures 3-5.**

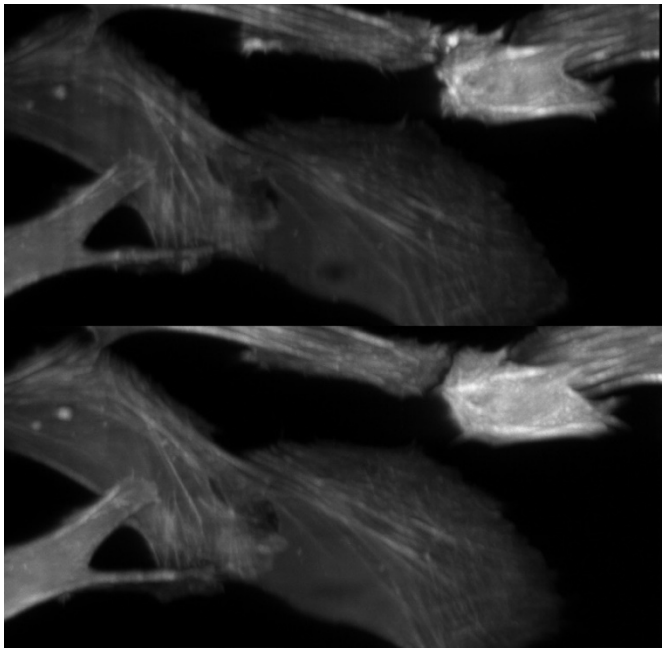

Supplementary Figure 2. Improved illumination homogeneity with resonantly scanned multidirectional illumination. Scattering, refraction, and absorption results in shadow and non-uniform illumination artifacts. By resonantly scanning the illumination beam in a plane conjugate to the sample, these artifacts are reduced substantially and thereby provide greater imaging quality.

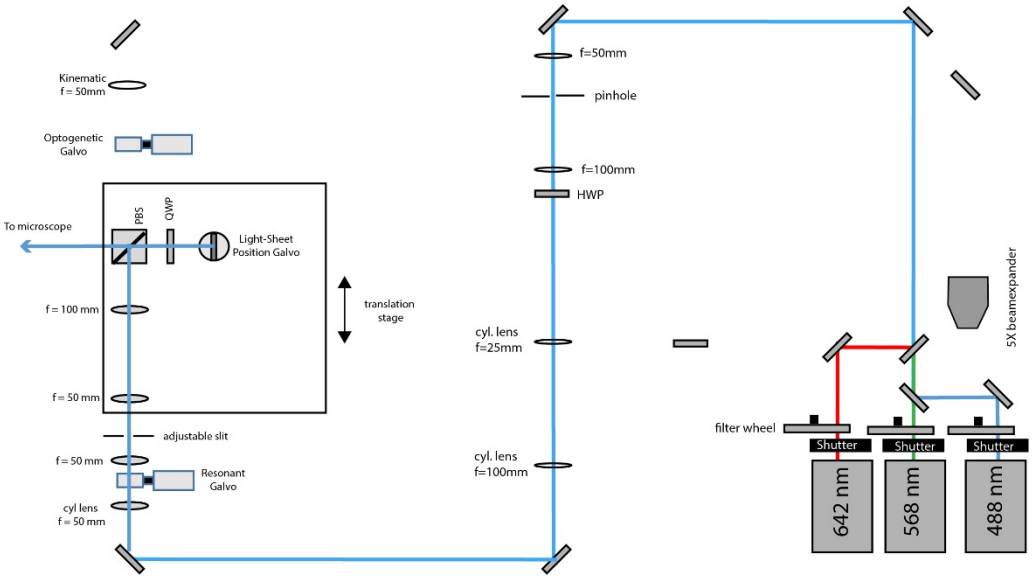

Supplementary Figure 3. Schematic diagram of the illumination unit configured for light-sheet illumination. 488nm, 568nm and 642nm laser light is combined by dichroic mirrors, but for clarity, only the blue laser path is outlined after laser combination. The light-sheet position galvo is conjugate to the pupil plane of the primary objective and allows fine adjustments of the relative position of the light-sheet to the focal plane of the tertiary imaging system.

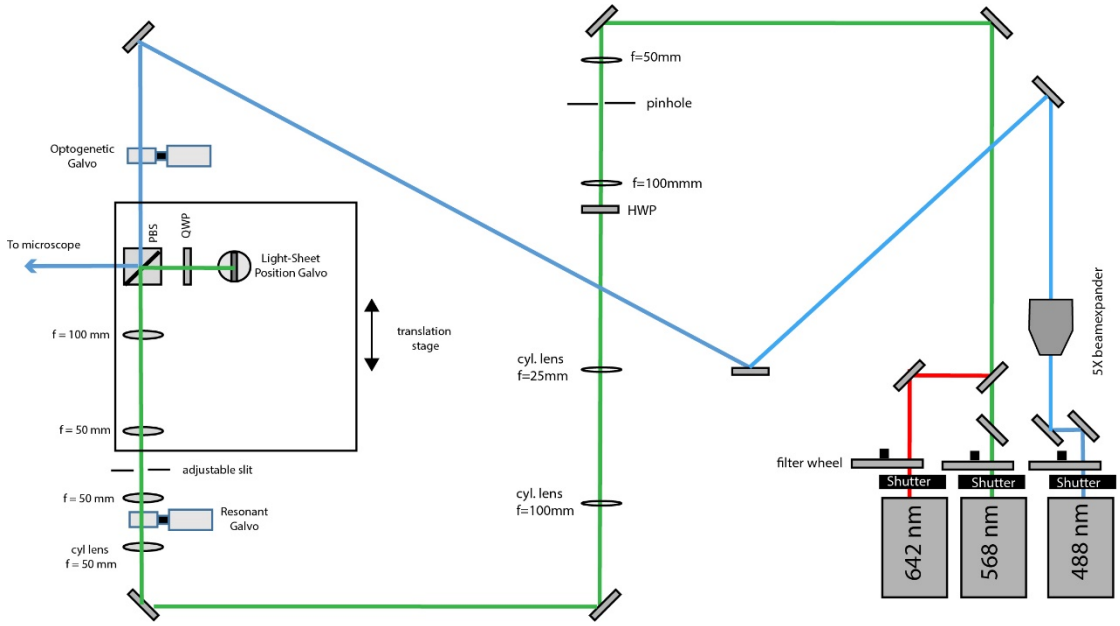

Supplementary Figure 4. Schematic diagram of the illumination unit configured for light-sheet illumination with the green and red laser and photo-activation with the blue laser. To this end, a flip mirror is used to send the 488nm laser light into a different beam path. The optogenetic galvo is conjugate to the pupil plane and allows lateral beam scanning.

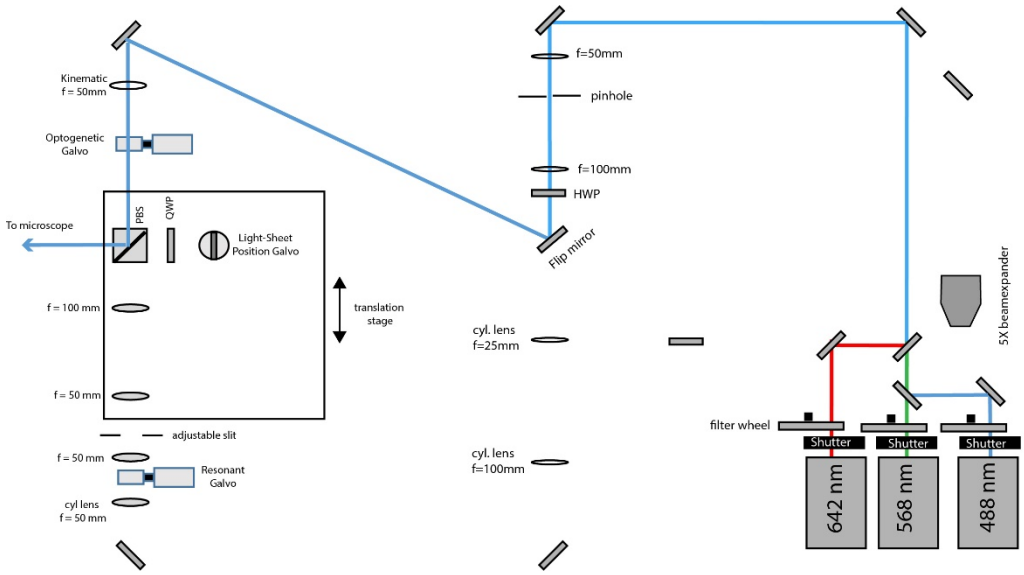

Supplementary Figure 5. Schematic diagram of the illumination unit configured for Widefield illumination. A flip mirror guides the light to the corresponding path and a kinematic mount inserts a lens to focus the laser beam on the optogenetic galvo (which is conjugated to the pupil plane of the primary objective), thereby producing a collimated laser beam in the sample space.

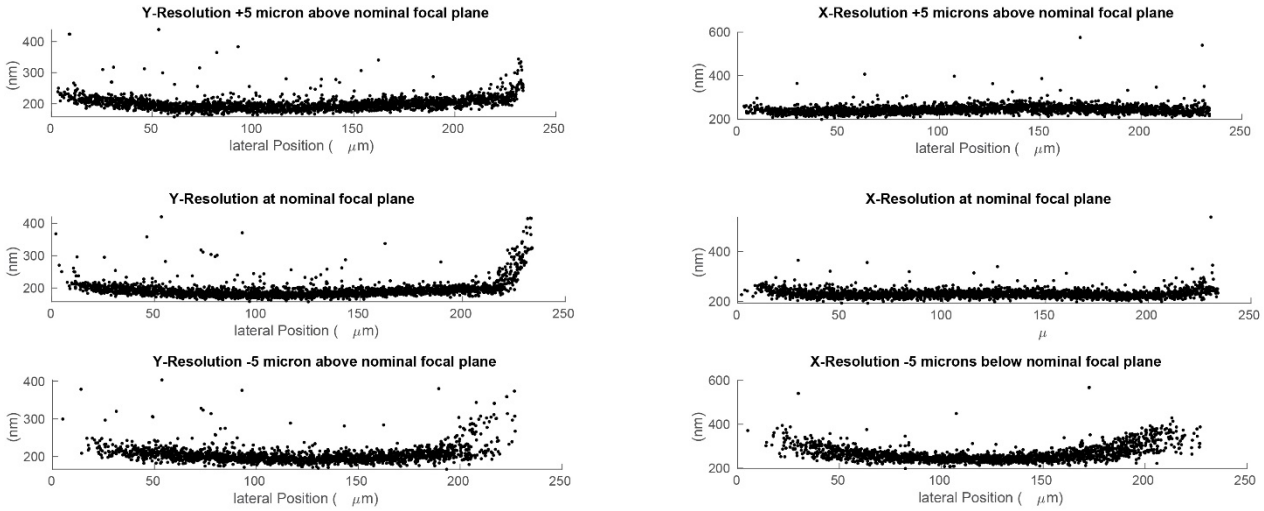

Supplementary Figure 6. Lateral resolution measured at different depth using 100 nm green fluorescent beads. Deconvolved data.

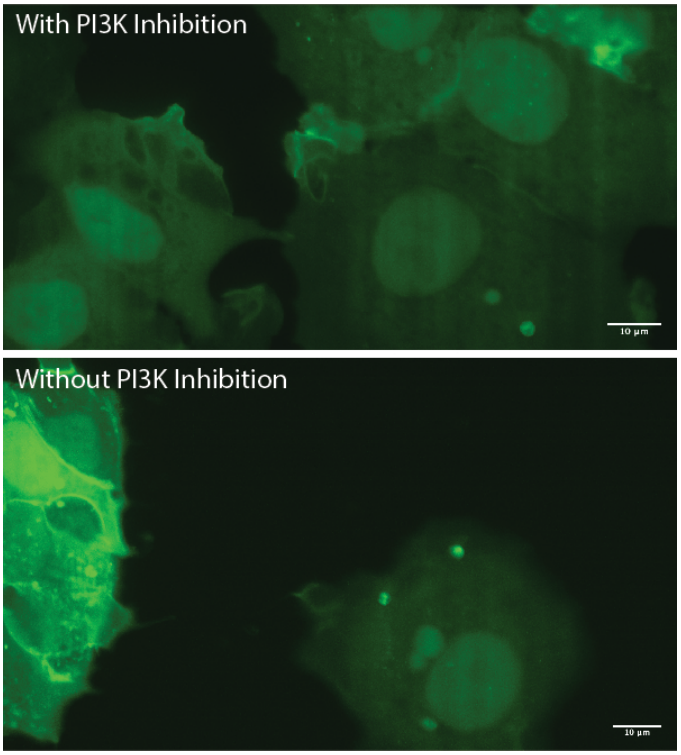

Supplementary Figure 7. PI3K activity in MCF7 breast cancer cells measured with the AktPH-GFP translocation biosensor, with and without treatment by the PI3Kα inhibitor alpelisib (1 μM alpelisib for 4 hours).

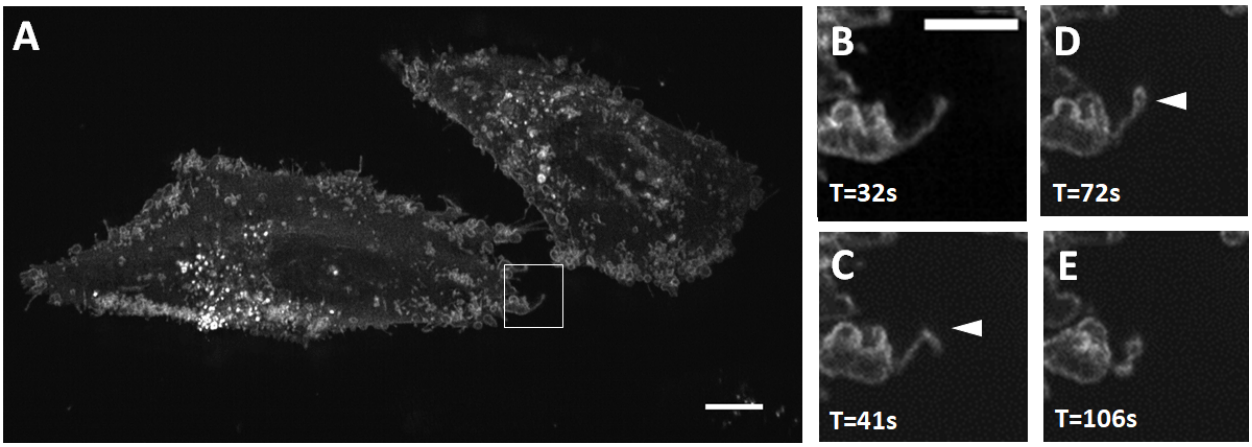

Supplementary Figure 8. (A) MV3 melanoma cells labeled with CAAX-Halo over 150 timepoints. (B-C) Magnified view of the boxed region in (A). Chevron points to a buckling event of a filopodia. (D-E) Magnified view of the boxed region shown in (A). Chevron points to a Bleb formation on the tip of a filopodia. Scale Bar: (A) 10 microns, (B) 5 microns.

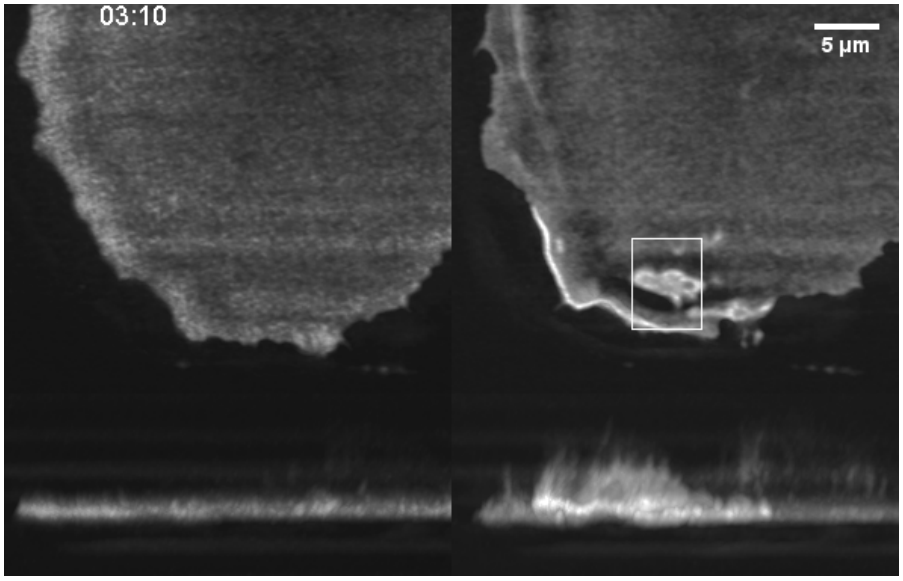

Supplementary Figure 9. MV3 cells expressing Cry2-iSH2 for PI3K photoactivaiton and SNAP-AktPH labeled with SNAP-Cell 647-SIR for PI3K visualization before (left) and during photoactivation (right) of PI3K acquired at 0.1 Hz; top shows maximum projection in XY and bottom shows maximum projection in XZ.

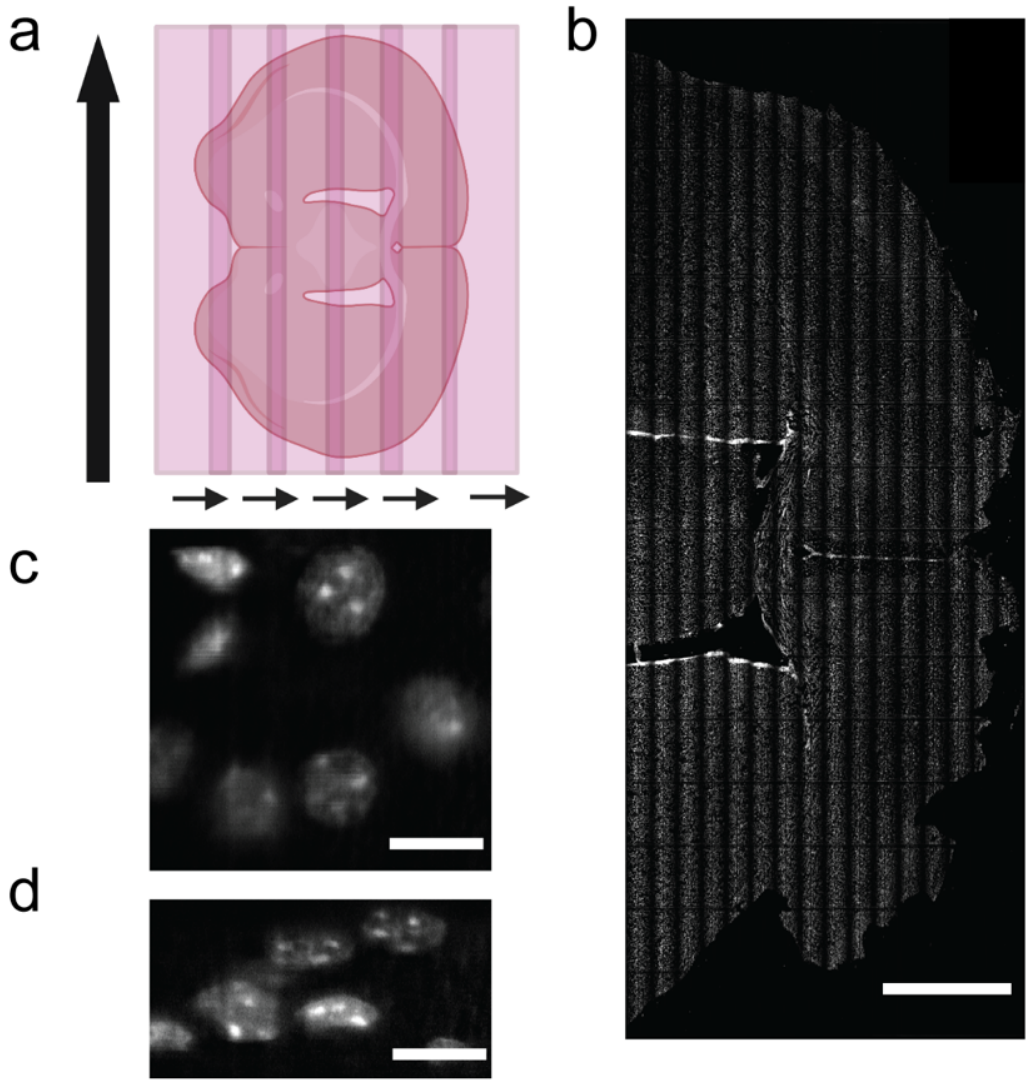

Supplementary Figure 10. Nuclei, imaged with DAPI, in a 30-micron thick slice of coronal mouse brain tissue. (A) Cartoon of stage-scanning strategy. (B) Maximum intensity projection of the tissue area imaged. Scale bar, 1 mm. (C) One slice from a small lateral section in the tissue. Scale bar, 10 microns. (D) Orthogonal projection of data shown in C. Scale bar, 10 microns.

Supplementary Tables

Figure	Sample	Label	Voxel Size (nm^3)	Volumetric Imaging Rate (Hz)	Post-Processing	Rendering Software
1C-D	100 nm beads	N/A	115x115x100			
2A	U2OS	EGFP-Sec61b	115x115x 250	1.19	Deconvolution + Histogram Matching	Imaris + Fiji
2B-C	RPE hTERT	mEmerald-Vimentin	115x115x100		Deconvolution	Fiji
2D-E	ARPE	EGFP-AP2	115x115x100	0.4	Deconvolution + Histogram Matching	Fiji
2F-H	MV3	CAAX-HALO	115x115x250	0.91	Deconvolution	Fiji
3	NK-92 + K562	LifeAct-mScarlet & LCK-mVenus	115x115x 250	0.09	Deconvolution + Histogram Matching	Fiji
4	1205Lu	EGFP-Tubulin & NLS-mScarlet	115x115x400	.05	Deconvolution	Fiji
5A	Cardiomyocytes	Fluo-3 AM	115x115x3000	10.4	Deconvolution+ Histogram Matching	Imaris
5B	MV3	GEMs-mSapphire	115x115x500	13.7	Deconvolution+ Histogram Matching	
6	MV3	AktPH-SNAP-A647	115x115x500	0.1	Deconvolution+ Histogram Matching	Imaris
S2		EGFP-Tractin	115x115x100			
S6	100 nm beads	N/A	115x115x100			
S7	MCF7	EGFP-AktPH				
S8	MV3	CAAX-HALO	115x115x00	115x115x250	Deconvolution	
S9	MV3	Cry2-iSH2 & SNAP-AktPH	115x115x250	0.1	Deconvolution + Histogram Matching	Imaris

Supplementary Table 1. Description of sample type, fluorescent labels, imaging conditions, data post-processing, and rendering, for each figure.

Primer	Sequence
EGFP-Forward	CCACTTCCTACCCTCGTAAAGTCGACATGGTGAGCAAGGGCGAGG
EGFP-Reverse	CTTGTACAGCTCGTCCATGCCGAG
Sec61b-Forward	CTCGGCATGGACGAGCTG
Sec61b-Reverse	CTGCAGGCTAGCCATATGACGCGTCTACGAACGAGTGTACTTGCCC
5' EcoRI-Forward	GCAGGAATTCATGGGATCAGATCCAAAAAAG
3'XbaI-Reverse	TGATTATGATCTAGAGTCGCG

Supplementary Table 2. Primer sequences used for PCR amplification.

Supplementary Movies

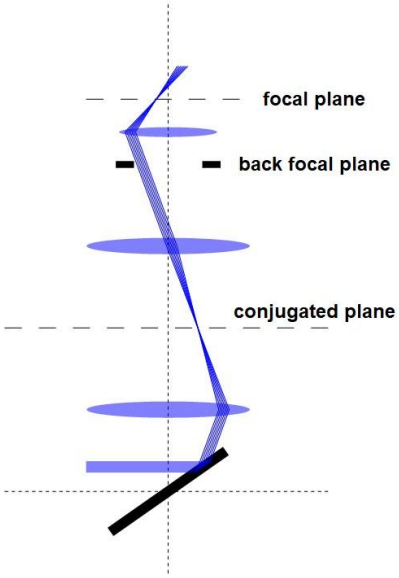

Supplementary Movie 1. Animation of light-sheet scanning and optogenetic activation. Blue rays represent the light-sheet illumination, and green rays indicate the diffraction-limited epi-illumination. Both beams are scanned with a mirror galvanometer (bottom) that is conjugate to the back focal plane of the primary objective (top).

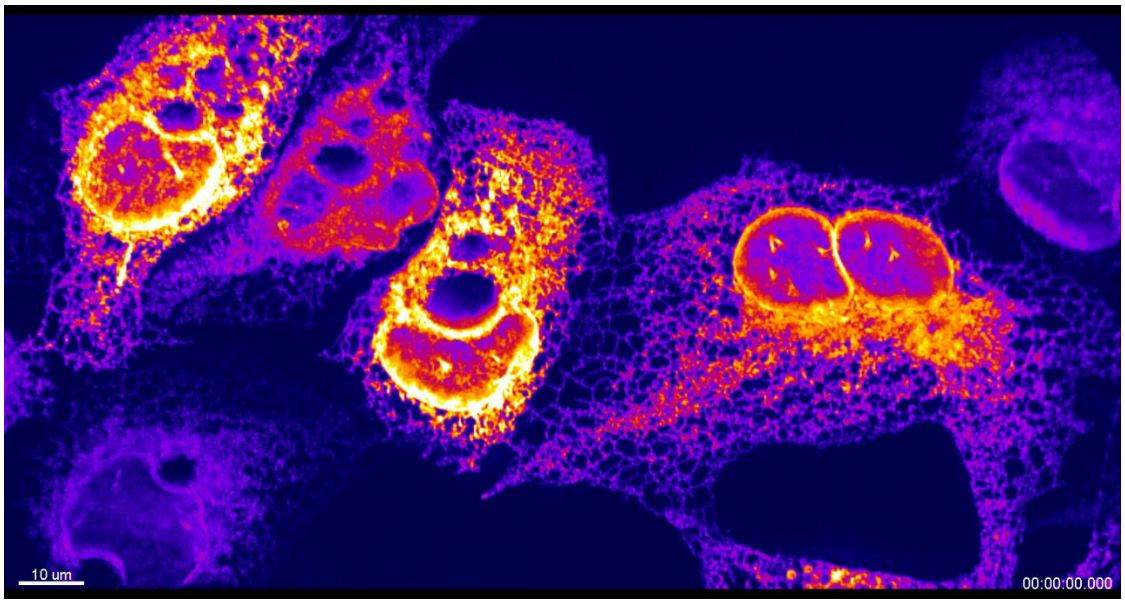

Supplementary Movie 2. Endoplasmic reticulum dynamics in osteosarcoma U2OS cells expressing Sec61-GFP. Time interval 0.84 seconds, scale bar, 10 microns.

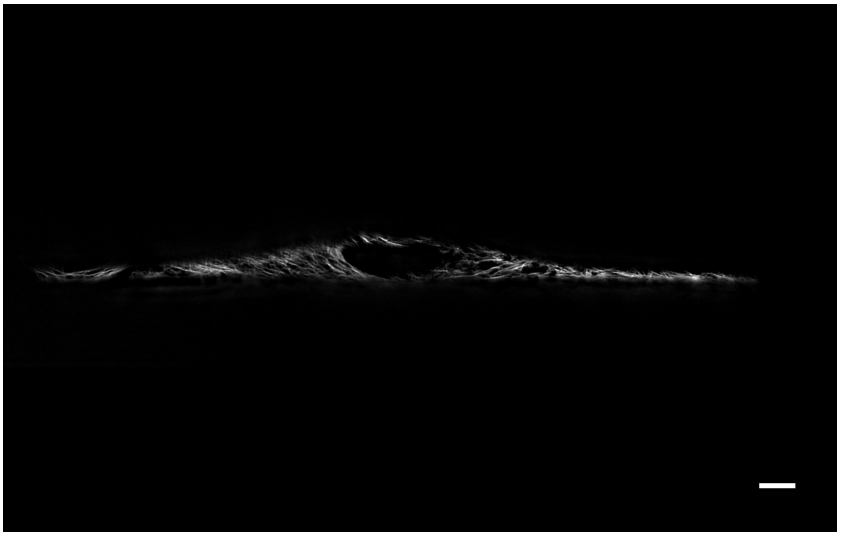

Supplementary Movie 3. 3D stack of RPE hTERT cells expressing GFP-vimentin. Data has been deconvolved and sheared into its proper Euclidian position. Scale bar, 20 microns.

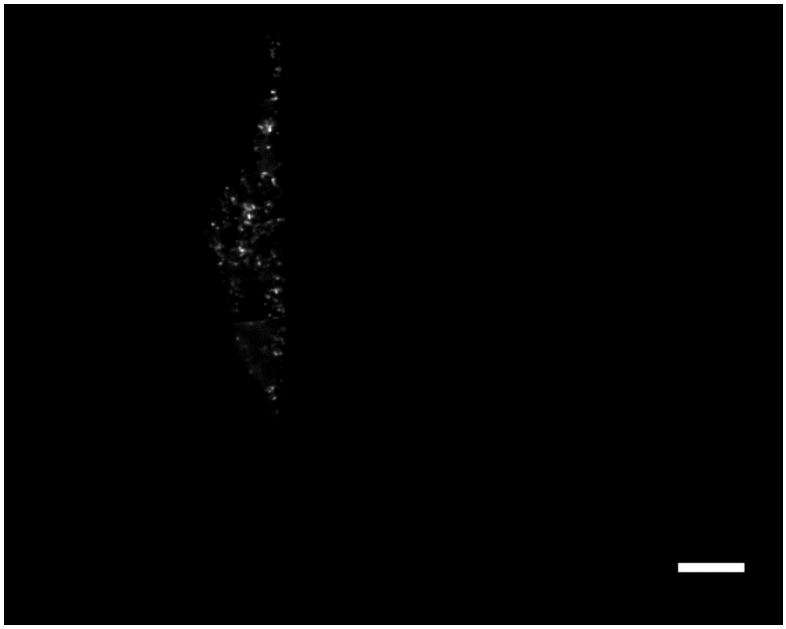

Supplementary Movie 4. 3D stack of ARPE cells tagged with AP2-GFP, a marker for clathrin-mediated endocytosis. Data has been deconvolved and sheared into its proper Euclidian position. Scale Bar: 10 microns.

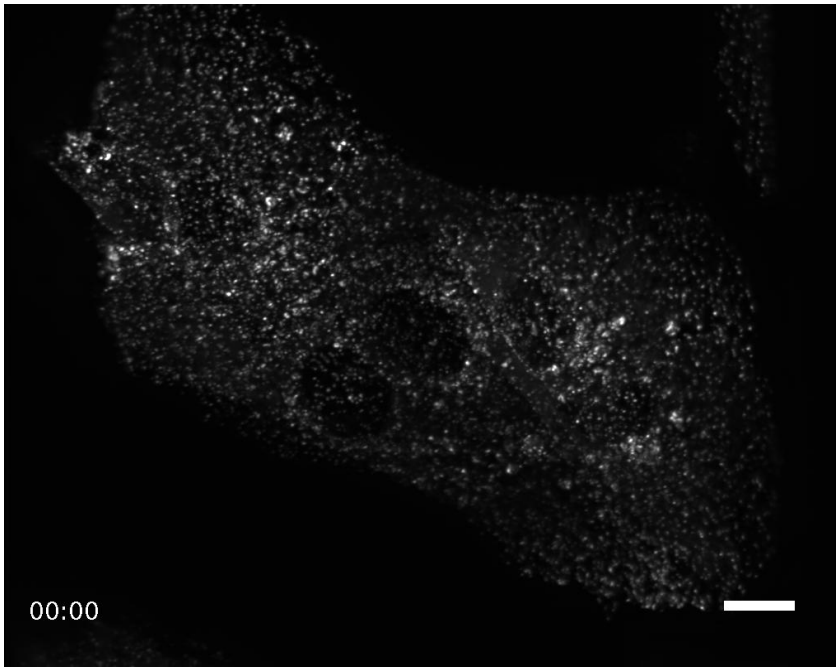

Supplementary Movie 5. Maximum intensity projection of ARPE cells tagged with AP2-GFP, a marker for clathrin-mediated endocytosis. Time interval 1.34 seconds, scale bar, 20 microns.

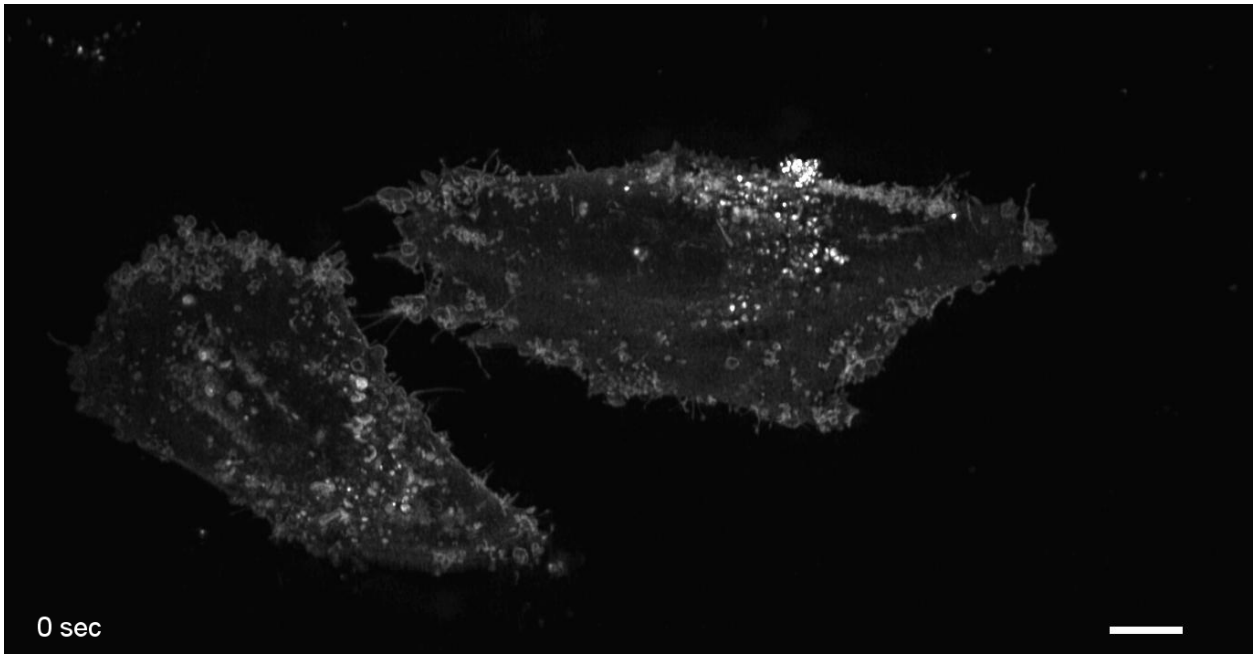

Supplementary movie 6. MV3 cells expressing the biorthogonal membrane marker, CAAX-Halo-Tag, labeled with Oregon Green. Time interval 1.09 s, scale bar 10 microns.

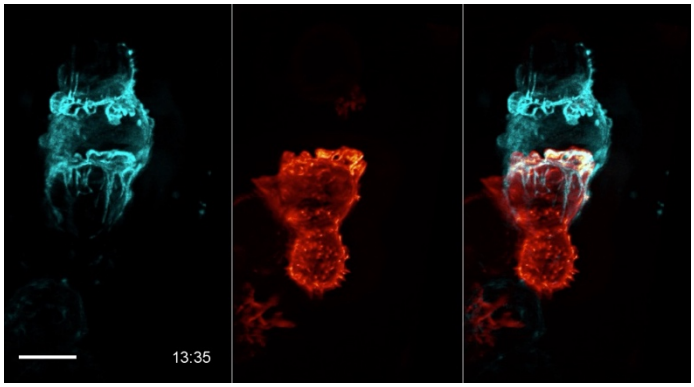

Supplementary Movie 7. An NK-92 natural killer cell forming an immunological synapse with a target cell. The NK-92 cell (Natural Killer cell line) was labeled with Life-Act-mScarlet, and is shown in orange. The target cell (K562 leukemia cell line) was labeled with Lck-mVenus, and is shown in cyan. Time interval 11.33 seconds, scale bar is 10 μm.

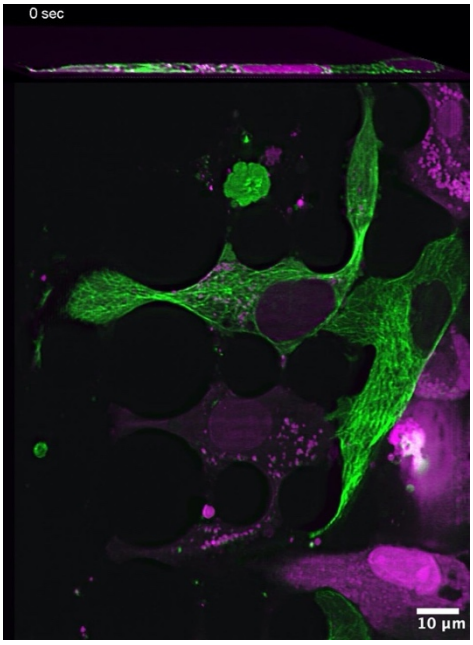

Supplementary Movie 8. 1250Lu metastatic melanoma cells expressing GFP-alpha-tubulin (green) and a 3x-NLS-mScarlet nuclear marker (cyan). Nuclei often undergo bending and rupture as cell migrate and squeeze through pillars. Time interval 29.88 seconds, scale bar 10 microns.

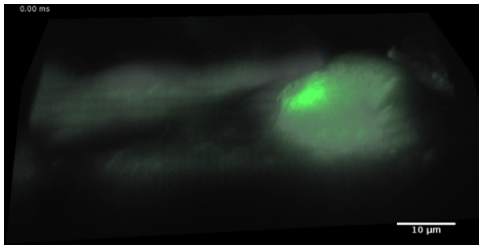

Supplementary movie 9. 3D rendering of primary cardiomyocyte stained with Fluo-3, a small-molecule sensor for Calcium (II). Green indicates fluctuations in intracellular calcium levels, and gray represents the

cell boundary (calculated as an average of all imaging frames). Time interval .096 seconds, scale bar 10 microns.

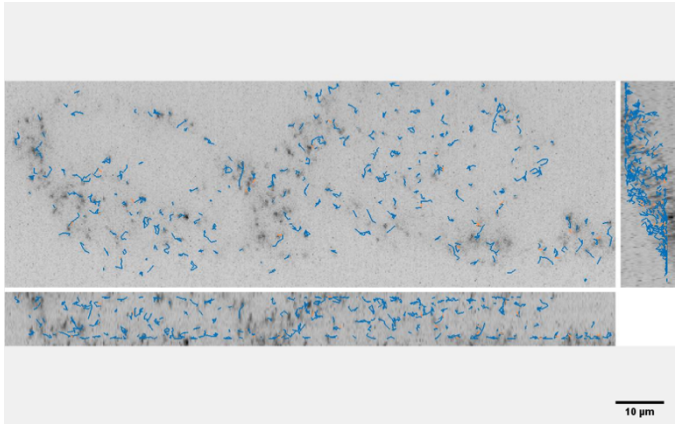

Supplementary Movie 10. Orthogonal maximum intensity projections of MV3 cells expressing cytosolic GEMs as rheological tracers. Particles were detected and tracked with the uTrack-3D software package. Time interval 0.073 seconds.

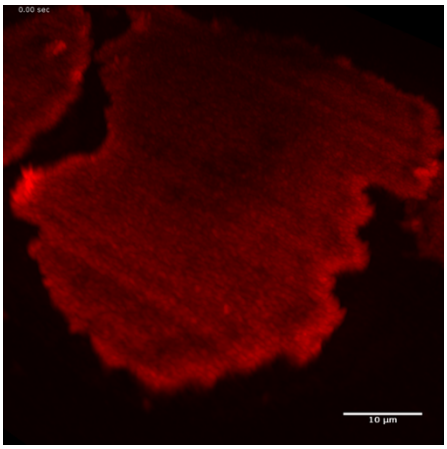

Supplementary Movie 11. 3D rendering of the cell shown in Figure 6 before and after photoactivation of PI3K.

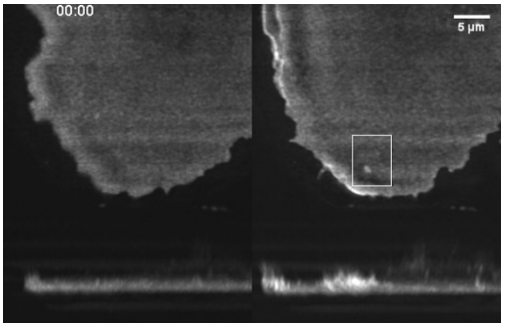

Supplementary Movie 12. XY and XZ maximum intensity projections of MV3 cells expressing a PI3K translocation biosensor (SNAP-AktPH labeled with SNAP-Cell-647 SiR) and the cry2-iSH2 localization to the membrane is shown. Time interval is 10s